Check for updates

Reconfigurable Intelligent Surfaces for Doppler Effect and Multipath Fading Mitigation

Ertugrul Basar*

Communications Research and Innovation Laboratory, Department of Electrical and Electronics Engineering, Koç University, Istanbul, Turkey

Owing to the envisioned new use-cases, such as immersive virtual reality and high-fidelity mobile hologram, and their potential challenging new requirements for future wireless networks, extensive research has already started on 6G and beyond wireless technologies. Despite the fact that several modern physical layer solutions have been introduced in the past decade, a level of saturation has been reached in terms of the available spectrum and adapted modulation/coding solutions, which accordingly limits the maximum capacity and reliability. Within this respective, reconfigurable intelligent surface (RIS)-empowered communication appears as a potential candidate to overcome the inherent drawbacks of legacy wireless systems. The core idea of RIS-assisted communication is the transformation of the random and uncontrollable wireless propagation environment into a reconfigurable communication system entity that plays an active role in conveying information and improving system performance. In this paper, the well-known multipath fading phenomenon is revisited in mobile wireless communication systems, and novel and unique solutions are introduced from the perspective of RISs. The feasibility of eliminating or mitigating the multipath fading effect stemming from the movement of mobile receivers is also investigated by utilizing RISs. It is shown that rapid fluctuations in the received signal strength due to the Doppler effect can be effectively reduced by using real-time tunable RISs. It is also proven that for a hypothetical propagation environment where all reflectors are coated with RISs, the multipath fading effect can be totally eliminated. Furthermore, we show that for more general propagation environments with several interacting objects, even a few real-time tunable RISs can remarkably reduce the Doppler spread and the deep fades in the received signal.

Keywords: 6G, Doppler effect, multipath fading, reconfigurable intelligent surface, intelligent reflecting surface

1. INTRODUCTION

Fifth generation (5G) wireless networks have three major use-cases with different user requirements, namely enhanced mobile broadband (eMBB), ultra-reliable and low-latency communications (URRLC), and massive machine type communications (mMTC). Although the introduction of promising physical layer (PHY) technologies in 5G, including millimeter wave (mmWave) communications, massive multiple-input multiple-output (MIMO) systems with hybrid precoding, and multiple orthogonal frequency division multiplexing (OFDM)

numerologies, the most recent mobile communication standards do not contain revolutionary ideas in terms of PHY solutions. Within this context, researchers have already started research on next-generation (6G) mobile technologies of 2030 and beyond by exploring completely new and radical PHY concepts to satisfy the requirements of the envisioned science-fiction like technologies. Although future 6G technologies might seem to be extensions of their 5G counterparts at this time (Gatherer, 2018), potential new user requirements, challenging use-cases, and new networking trends of 6G (Saad et al., 2020) will bring more challenging problems in mobile wireless communication, which necessitate radically new PHY concepts for next-generation radios. New solutions for 6G any beyond must provide extremely high energy and spectral efficiencies along with ultra-reliability and ultra-security. Furthermore, we need a highly flexible and controllable PHY concept to satisfy the challenging requirements of the envisioned use-cases. Despite the intensive research efforts in the field of PHY research during the past two decades, these are still features that we seek for in state-of-the-art wireless communication systems and standards, which might necessitate a rethink of communication system design for 6G and beyond.

Due to the random and uncontrollable behavior of wireless propagation, it has always been challenging for the network operators to build ubiquitous wireless networks that can provide high quality-of-service (QoS) and uninterrupted connectivity to multiple users and devices in the presence of harsh propagation environments since the early wireless networks (Molisch, 2011). Particularly, this challenging behavior of wireless propagation causes

  (i) *deep fading* due to uncontrollable interactions of transmitted waves with surrounding objects and their constructive and destructive interference at the receiver,
 (ii) *severe attenuation* due to high path loss and transmissions under blocked line-of-sight (LOS) links (shadowing),
(iii) *inter-symbol interference* due to different runtimes of multipath components relative to the symbol period, and
(iv) *Doppler effect* due to the high mobility of users and/or surrounding objects.

Although a plethora of modern PHY solutions, including multi-carrier modulation, adaptive modulation and coding, non-orthogonal multiple access, relaying, beamforming, massive MIMO, and reconfigurable antennas, have been considered to overcome these challenges in the next several decades, the overall progress in terms of the PHY improvement has been still relatively slow. This can be explained by the following undeniable fact in wireless systems: *the propagation environment has been perceived as a randomly behaving entity until the start of the modern wireless communications era and it degrades the overall received signal quality and the communication QoS owing to the uncontrollable interactions of the transmitted signals with the surrounding objects.* In other terms, the primary focus of system designers has always been the transmitter and receiver ends of communication systems to cope with the negative effect of the wireless channel, which is inherently assumed to an uncontrollable part of communication systems. One of the main objectives of this paper is to challenge this view by exploiting the new paradigm of intelligent communication environments.

In recent years, reconfigurable intelligent surfaces (RISs) have been brought to the attention of the wireless research community to enable the control of wireless environments (Basar et al., 2019; Di Renzo, 2019). RISs are artificial and 2D surfaces of electromagnetic (EM) material that are electronically controlled with integrated electronics. By modifying the current distribution over themselves in a deliberate manner, RISs might support unique EM functionalities, including anomalous reflection, wave absorption, polarization modification, wave splitting, wave focusing, and phase modification. Recent practical efforts in the literature have revealed that these unique EM functionalities are possible with a very simple architecture that does not require complex decoding, encoding, and radio frequency (RF) processing operations and the communication QoS (capacity, signal power, secrecy, error performance, etc.) can be boosted by exploiting the implicit randomness of wireless propagation (Basar et al., 2019). However, the fundamental issues remain unsolved within the theoretical and practical understanding as well as modeling of RIS-aided communication systems.

Contrary to traditional wireless networks, where the wireless communication environment is out of control of the system designers, the emerging concept of smart radio environments have been realized by RISs. Here, the propagation environment is turned into an intelligent and controllable system entity that plays an active role in processing signals and accordingly, transferring information in an effective way. It is worth noting that the introduction of controllable propagation is a completely new paradigm in wireless communication and has the potential to change the way the communication takes place. The core technology behind this new concept is RISs, which are the 2D equivalent of metamaterials (metasurfaces). It is worth noting that RIS-empowered communication is completely different from other well-known technologies, such as MIMO beamforming, amplify-and-forward relaying, passive reflect-arrays, and backscatter communications, which are currently employed in wireless networks. On the other hand, RIS-assisted systems have the following major distinguishable features and advantages:

  (i) RISs do not require an energy source for RF signal processing thanks due their almost passive architecture;
 (ii) RISs provide an inherently full-duplex transmission and do not amplify or introduce noise when reflecting the signals due to their passive natures;
(iii) RISs can be easily deployed on certain locations, such as the facades of buildings, ceilings of factories, and indoor walls;
(iv) RISs are reconfigurable and can adapt themselves according to the changes of the wireless environment.

These distinctive characteristics make RIS-empowered communication a unique technology and introduce important communication theoretical as well as system design challenges, some of which will be tackled in this paper.

Within the context of radical PHY solutions toward beyond 5G wireless networks, there has been a growing recent interest

in novel signaling and modulation concepts in which the propagation environment is controlled or its inherently random nature is exploited to further increase the spectral/energy efficiency and/or QoS of target communication systems. For instance, IM-based (Basar, 2016; Basar et al., 2017) schemes, such as media-based modulation (Khandani, 2013; Basar, 2019a) and spatial scattering modulation (Ding et al., 2017) benefit from reconfigurable antennas or scatterers in the environment to create different signatures for received signals in rich scattering environments and transmit additional information bits accordingly. On the other hand, RISs primarily focus on the control of the propagation environment by exploiting reconfigurable reflectors/scatterers embedded on themselves to boost the signal quality at the receiver. It is worth noting that a number of preliminary works have been reported in the earlier literature to control or benefit from wireless propagation, such as intelligent walls (Subrt and Pechac, 2012a,b), spatial microwave modulators (Kaina et al., 2014), 3D reflectors (Xiong et al., 2017), and coding metamaterials (Cui et al., 2014). Nevertheless, the rise of RIS-empowered intelligent communication environments can be mainly attributed to programmable (digitally-controlled) metasurfaces (Yang et al., 2016), reconfigurable reflect-arrays (Tan et al., 2016, 2018), software-controlled hypersurfaces (Liaskos et al., 2018), and intelligent metasurfaces (Liu et al., 2019). For instance, the intelligent metasurface design of Liu et al. (2019), enables tunable anomalous reflection as well as perfect absorption by carefully adjusting the resistance and the capacitance of its unit cells at 5 GHz.

The concept of RIS-empowered wireless communication has received tremendous interest from researchers in our community in the past couple of years due to interesting as well as challenging problems it brings in the context of metamaterials and electromagnetics, communication, optimization, and probability theories (Basar et al., 2019; Di Renzo, 2019; Wu and Zhang, 2019b; Di Renzo et al., 2020). Particularly, researchers focused on

(i) maximization of the achievable rate, minimum signal-to-interference-plus noise ratio (SINR), and energy efficiency and minimization of the transmit power by joint optimization of the RIS phases and the transmit beamformer (Huang et al., 2018a,b, 2019; Wu and Zhang, 2018; Yu et al., 2019b; Nadeem et al., 2020),

(ii) maximization of the received signal-to-noise ratio (SNR) to minimize the symbol error probability (Basar, 2019b),

(iii) efficient channel estimation techniques with passive RIS elements as well as deep learning tools to reduce the training overhead and to reconfigure RISs (Mishra and Johansson, 2019; He and Yuan, 2020; Taha et al., 2021),

(iv) PHY security solutions by joint optimization of the transmit beamformer and RIS phases (Chen et al., 2019; Cui et al., 2019; Yu et al., 2019a),

(v) practical issues, such as erroneous reflector phases, realistic phase shifts, and discrete phase shifts (Wu and Zhang, 2019a; Abeywickrama et al., 2020; Badiu and Coon, 2020),

(vi) design of NOMA-based systems for downlink transmit power minimization and for the minimum decoding SINR maximization of all users (Ding and Poor, 2019; Fu et al., 2019),

(vii) channel modeling and measurements for different frequency bands and RIS types (Tang, 2019; Basar and Yildirim, 2020a,b,c; Danufane et al., 2020; Yildirim et al., 2020), and

(viii) practical implementations (Dai et al., 2020, 2021).

Furthermore, the first attempts on combining RISs with space modulation, visible light and free space optical communications, unmanned aerial vehicles, wireless information and power transfer systems, and OFDM systems have been reported in recent times (see Basar et al., 2019; Di Renzo et al., 2020; Wu et al., 2020 and references therein).

In our paper, we take a step back and revisit the well-known phenomenons of multipath fading and Doppler effect in mobile communications from the perspective of emerging RISs. Although the potential of RISs has been explored from many aspects as discussed above, to the best of our knowledge, their potential in terms of Doppler effect mitigation has not been fully understood yet. For this purpose, by following a bottom-up approach from simple networks to more sophisticated ones, we explore the potential of RISs to eliminate multipath fading effect stemming from Doppler frequency shifts of a mobile receiver for the first time in the literature. Specifically, we prove that the rapid fluctuations in the received signal strength due to the user movement can be effectively eliminated and/or mitigated by utilizing real-time tunable RISs. We introduce a number of novel and effective methods that provide interesting trade-offs between Doppler effect mitigation and average received signal strength maximization, for the reconfiguration of the available RISs in the system and reveal their potential for future mobile networks.

It is worth noting that the results in this paper are obtained for hypothetical RISs which create specular reflections with a single and very large conducting element. However, the results obtained in this paper can be adapted for practical RISs in which many number of tiny elements on them scatter the incoming signals in all directions, in other words, for RISs with multiplicative path loss terms. Finally, it has been also shown that by using carefully positioned and relatively large RISs, it might be possible to reach the same path gain as that of specular reflection by carefully adjusting the phases of RIS elements (Ellingson, 2019). Nevertheless, exploration of application scenarios in which practical RISs might be effectively used to overcome Doppler and multipath effects is an open problem and this paper aims to shed light in this direction by following a unified signal processing perspective.

The rest of the paper is organized as follows. In section 2, we consider a simple two-path scenario and revisit multipath and Doppler effects. In section 3, we deal with Doppler effect elimination with RISs. More sophisticated networks with multiple RISs and objects as well as practical issues are covered under **Supplementary Material**. Finally, we conclude the paper in section 4.

2. REVISITING MULTIPATH AND DOPPLER EFFECTS WITH SIMPLE CASE STUDIES

In this section, we revisit the Doppler and multipath fading effects caused by the movement of a mobile receiver under a simple propagation scenario (with and without an RIS). We focus our attention to the low-pass equivalent and noise-free received signals while a generalization to pass-band signaling is straightforward from the given low-pass equivalent signals.

2.1. Multipath Fading Due to User Movement and A Reflector

In this subsection, we focus on the basic two-path propagation geometry given in **Figure 1** with a base station (BS), a mobile station (MS) and an interacting object (IO) (Basar, 2020). In this geometry, the MS has a constant speed of V (in m/s) and it follows a straight route toward the IO. Here, a second replica of the transmitted signal, reflected from the IO, arrives at the receiver of the MS in addition to the signal traveled through the LOS path between two terminals. For simplicity, a reflection coefficient of unity magnitude and phase π is assumed for the IO, that is, $R = -1$. In this setup, the reflecting surface is assumed to be large and smooth enough to create specular reflections.

To capture the effects of multipath fading and Doppler in the received signal with respect to the motion of the MS in time, the transmission of an unmodulated radio frequency (RF) carrier signal $\cos(2\pi f_c t + \Theta_0)$ is assumed, where f_c is the carrier frequency and Θ_0 is the initial phase. This carrier signal is equivalent to $x(t) = \exp(j\Theta_0)$ in complex baseband representation. Here, we focus on a very short travel distance (a few wavelengths) in order to illustrate the fade pattern and the Doppler spectrum due to the movement of the MS. As a result, the received direct and reflected signals have almost constant amplitudes during our observation, while experiencing rapidly varying phase terms. In other words, focusing on a very short time interval ensures that the large-scale fading does not affect the received signal. At the same time, we observe Doppler shifts at the received signals due to the movement of the MS. Against this background, we obtain the received complex envelope as (Fontan and Espineira, 2008).

$$r(t) = \frac{\lambda}{4\pi}\left(\frac{e^{-j\frac{2\pi d_{\mathrm{LOS}}(t)}{\lambda}}}{d_{\mathrm{LOS}}(t)} - \frac{e^{-j\frac{2\pi d_R(t)}{\lambda}}}{d_R(t)}\right) \qquad (1)$$

where the initial carrier phase Θ_0 is dropped for clarity. Here $d_{\mathrm{LOS}}(t)$ and $d_R(t)$, respectively denote the time-varying radio path distances for the BS-MS and the BS-IO-MS links due to the movement of the MS. For this specific setup in **Figure 1**, we have $d_{\mathrm{LOS}}(t) = d_{\mathrm{LOS}} + Vt$ and $d_R(t) = d_{\mathrm{LOS}} + 2d_1 - Vt$, where d_{LOS} and d_1, respectively stand for the initial BS-MS and MS-IO distances. We further assume a horizontal communication link between the BS and the MS owing to their sufficiently small antenna height differences. The same assumption applies to the reflected signal stemming from the IO. In other words, MS travel distance variations directly affect radio path lengths of both rays. However, a generalization is straightforward for signals

FIGURE 1 | Two-ray propagation model with a mobile station and an IO creating reflections.
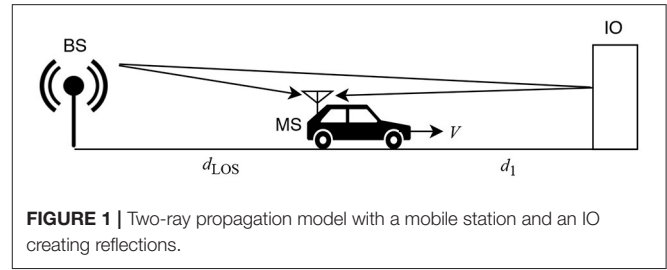
coming from different angles (see **Supplementary Section 1**). As mentioned earlier, we focus into only a few wavelengths of travel distance of the MS (a very short time interval) to purely focus on small-scale fading effects, while due to this short distance, two rays have approximately constant amplitudes for all positions of the MS. In light of these assumptions in the system model, (1) simplifies to

$$r(t) = \frac{\lambda}{4\pi}\left(\frac{e^{-j2\pi f_D t - j\phi_{\mathrm{LOS}}}}{d_{\mathrm{LOS}}} - \frac{e^{j2\pi f_D t - j\phi_1}}{d_{\mathrm{LOS}} + 2d_1}\right) \qquad (2)$$

where $f_D = V/\lambda$ is Doppler shift with respect to the nominal carrier frequency in the passband or with respect to 0 Hz in low-pass equivalent representation, $\phi_{\mathrm{LOS}} = 2\pi d_{\mathrm{LOS}}/\lambda$, and $\phi_1 = 2\pi(d_{\mathrm{LOS}} + 2d_1)/\lambda$. The constant (initial) phase terms of ϕ_{LOS} and ϕ_1 can be readily dropped if they are integer multiples of 2π. In light of this, using the properties of complex exponentials,[1] the magnitude of the complex envelope can be obtained as follows:

$$|r(t)| = \left(\frac{\lambda}{4\pi}\right)\left(\frac{1}{d_{\mathrm{LOS}}^2} + \frac{1}{(d_{\mathrm{LOS}} + 2d_1)^2} - \frac{2\cos(4\pi f_D t)}{d_{\mathrm{LOS}}(d_{\mathrm{LOS}} + 2d_1)}\right)^{1/2}. \qquad (3)$$

In **Figure 2**, the magnitude of the complex envelope in (3) is plotted for the travel of the MS for six wavelengths (which corresponds to an observation time of 0.06 s for the given MS speed) considering the following system parameters[2]: $f_c = 3$ GHz, $V = 10$ m/s with different d_{LOS} and d_1 values for a fixed BS-IO total distance of $d_{\mathrm{LOS}} + d_1 = 2,000$ m. As seen from **Figure 2**, the received signal strength fluctuates rapidly around a mean value that is dictated by the path loss, due to the destructive and constructive interference of arriving two signals. We further note that this fluctuation in the signal envelope has a frequency of $2f_D$ Hz as evident from (3). This oscillation is also known as the *fade pattern* of the received signal's envelope. We also note that the variation of the magnitude is more significant for smaller d_1 values, when the values of $d_{\mathrm{LOS}}(t)$ and $d_R(t)$ are close to each other, which corresponds a stronger interference between multipaths. This is also verified by the Doppler spectrum

---

[1]For $z_1 = r_1 e^{j\xi_1}$, $z_2 = r_2 e^{j\xi_2}$, and $z_3 = z_1 + z_2 = r_3 e^{j\xi_3}$, we have $r_3 = (r_1^2 + r_2^2 + 2r_1 r_2 \cos(\xi_1 - \xi_2))^{1/2}$.
[2]The same simulation parameters (mobile speed, carrier frequency, observation interval, traveled distance, FFT size, sampling distance and time) are used in the following unless specified otherwise.
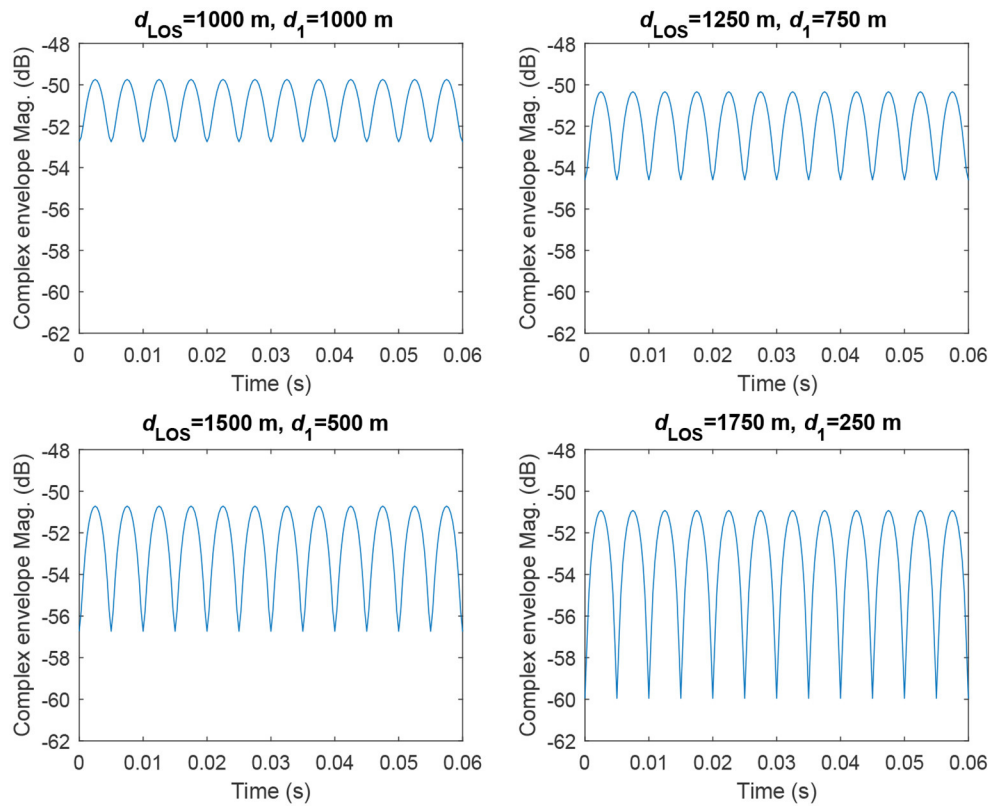
FIGURE 2 | Complex envelope variation with respect to MS movement with $V = 10$ m/s for varying d_{LOS} and d_1 (observation interval: 0.06 s, traveled distance: $6\lambda = 0.6$ m).

of the received signal given in **Figure 3** for these four cases, which include two sharp components at opposite frequencies, i.e., $-V/\lambda = -100$ Hz (from the LOS path) and $V/\lambda = 100$ Hz (from the IO) with different normalized amplitudes due to different travel distances of the two rays.

2.2. Eliminating Multipath Fading Due to User Movement With an RIS

In this subsection, we focus on the same basic system model of subsection 2.1 (**Figure 1**), however, we consider that the IO creates a controllable reflection at this time, thanks to the RIS that is mounted on its facade with the purpose of manipulating the reflected signals. In this setup, we capture the intelligent reflection from the RIS by a time-varying but unit gain (passive) reflection coefficient, which is denoted by $R(t) = e^{j\theta(t)}$. Here $\theta(t)$ stands for the time-varying reflection phase of the RIS. In light of this, the received complex envelope is expressed as

$$r(t) = \frac{\lambda}{4\pi} \left(\frac{e^{-j2\pi f_D t}}{d_{\text{LOS}}} + \frac{e^{j2\pi f_D t + j\theta(t)}}{d_{\text{LOS}} + 2d_1} \right). \qquad (4)$$

From (4), one can easily observe that the magnitude of $r(t)$ can be maximized when the phases of multipath components (direct and reflected signals) are perfectly aligned, that is, by adjusting the time-varying RIS phase as $\theta(t) = -4\pi f_D t \pmod{2\pi}$. We note

that the maximization of $|r(t)|$ can only be feasible with a unique RIS, which can adjust its reflection phase in a dynamic manner with respect to time, in accordance with the user movement. The practical issues related to this adjustment procedure are discussed in **Supplementary Material**. With the determined value of $\theta(t)$ discussed above, the complex envelope of the received signal simplifies to

$$r(t) = \frac{\lambda e^{-j2\pi f_D t}}{4\pi} \left(\frac{1}{d_{\text{LOS}}} + \frac{1}{d_{\text{LOS}} + 2d_1} \right). \qquad (5)$$

As seen from (5), the magnitude of the complex envelope is now maximized. Furthermore, it remains constant with respect to time can be given in the following:

$$|r(t)|_{\text{max}} = \frac{\lambda}{4\pi} \left(\frac{1}{d_{\text{LOS}}} + \frac{1}{d_{\text{LOS}} + 2d_1} \right). \qquad (6)$$

In light of (5) and (6), we have the following three remarks.

Remark 1: The multipath fading effect (rapid fluctuations in the received signal strength) can be eliminated by time-varying intelligent reflection of the RIS for the scenario of **Figure 1**. In this case, we obtain a constant magnitude for the received complex envelope, which is also shown in **Figure 4A**. In other words, by utilizing a unique RIS with a time-varying reflection
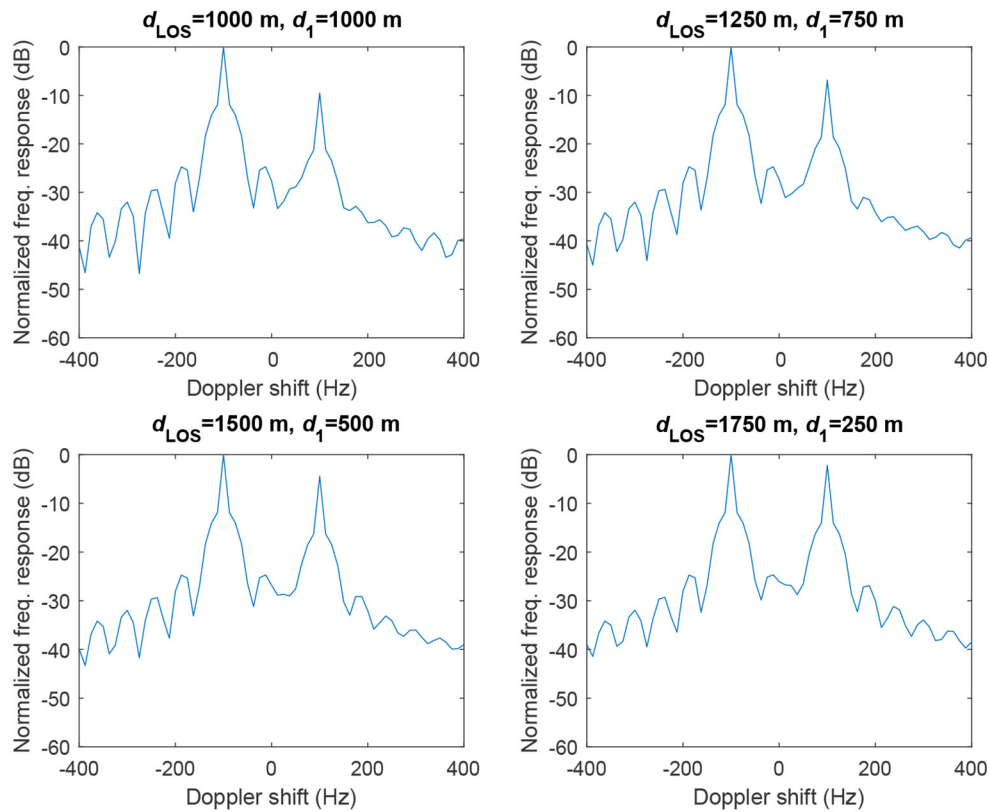
FIGURE 3 | Doppler spectrum of the received signal for varying d_{LOS} and d_1 (FFT size: 256, sampling distance: $\lambda/32 = 0.003125$ m, sampling time: $\lambda/(32 \times V) = 0.3125$ ms).

phase, one can escape from rapid fluctuations in the received signal due to the user movement. For this setup, the position of the RIS can be arbitrarily selected as long as the RIS is adjusting the reflection phase in real-time. We further note that a maximized complex envelope magnitude improves the received signal-to-noise-ratio, in return, the achievable capacity.

Remark 2: The received signal is still subject to a Doppler shift of $-f_D$ Hz, which is also observed from the Doppler spectrum of **Figure 4B**. Although the RIS effectively eliminates fade patterns, due to the direct signal received from the BS, which is out of the control of the RIS, it is not possible to eliminate Doppler frequency shifts in this propagation scenario.

Remark 3: For the case of a practical RIS in which the incoming signals are scattered with many number of tiny RIS elements in **Figure 1**, the received complex envelope is obtained as

$$r(t) = \frac{\lambda}{4\pi d_{LOS}} e^{-j2\pi d_{LOS}(t)/\lambda} + \sum_{n=1}^{N} \frac{\lambda^2 G_e}{(4\pi)^2(d_{LOS} + d_1)d_1}$$
$$e^{j(\theta_n(t) - 2\pi d_{R_n}(t)/\lambda)} \quad (7)$$

where G_e is the element gain, $\theta_n(t)$ is the adjustable phase of the nth RIS element and $d_{R_n}(t)$ is the associated path length (Basar and Yildirim, 2020b). Here, under the case of far-field, the same

path loss is assumed for all RIS elements. By carefully adjusting the RIS phases, that is, for $\theta_n(t) = 2\pi(d_{R_n}(t) - d_{LOS}(t))/\lambda$, the signals coming from the RIS can be aligned to the LOS signal and the magnitude of the complex envelope can be kept constant. Please note that by carefully positioning the RIS and adjusting its size, the magnitude of the complex envelope can be maximized by overcoming the multiplicative path loss in (7). In other words, the maximization of the received complex envelope, as well as the effectiveness of the RIS, is not only dependent on time-varying RIS phases, but also its position relative to the transmitter and/or MS due to the multiplicative path loss in (7). Due to the broad scope of the current paper, detailed investigation of RISs with many scattering elements is left as a future study, while the presented results can be generalized in a systematic way.

2.3. Increasing Fading and Doppler Effects With an RIS

So far, we focused our attention on the maximization of the received signal strength for the scenario of **Figure 1**, by carefully adjusting the RIS reflection phase in real time. On the contrary, it might be possible to intentionally degrade the received signal strength as well as increase the Doppler spread for an unintended mobile receiver or for an eavesdropper. Based on the received signal model of (4), when the received two signals are in-phase, we obtain the maximum magnitude for the received signal as
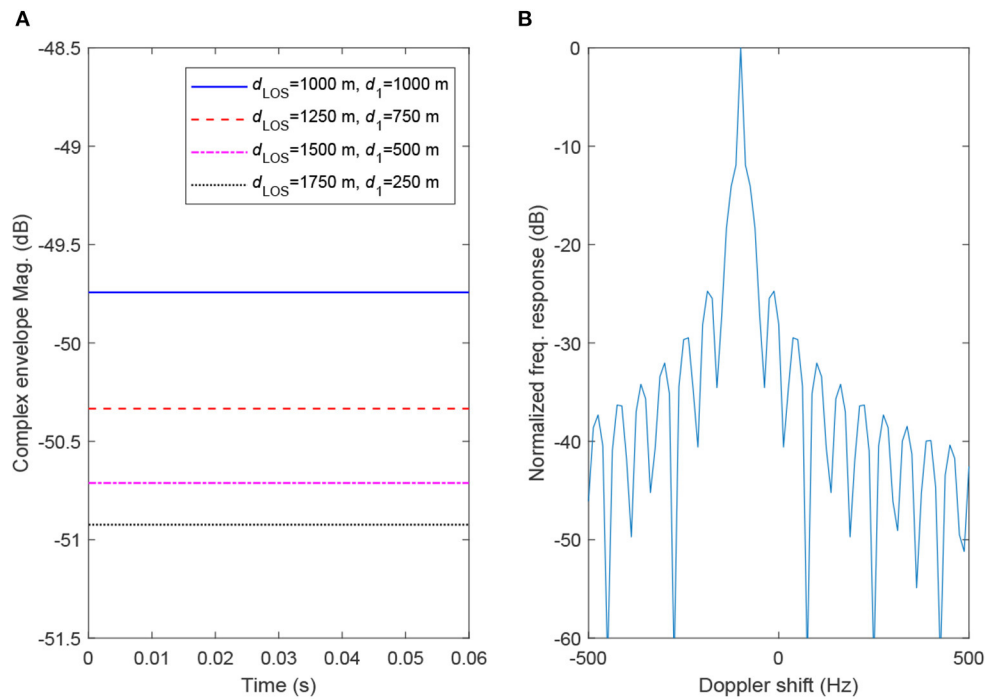
FIGURE 4 | **(A)** Maximized magnitude of the received signal in the presence of an RIS, **(B)** Doppler spectrum of the received signal for all scenarios.

in (6). On the other hand, adjusting the RIS reflection phase as $\theta(t) = -4\pi f_D t + \pi$ (mod 2π), we obtain completely out-of-phase two arriving signals, and the resulting minimum complex envelope magnitude becomes

$$|r(t)|_{\min} = \frac{\lambda}{4\pi} \left(\frac{1}{d_{\mathrm{LOS}}} - \frac{1}{d_{\mathrm{LOS}} + 2d_1} \right). \qquad (8)$$

As seen from (8), the degradation in the received signal strength would be more noticeable for smaller d_1. However, the magnitude of the complex envelope becomes constant as in (6), i.e., no fade patterns are observed. In **Figure 5A**, we depict the minimized complex envelope magnitudes by intentionally out-phasing the direct and reflected signals for varying d_{LOS} and d_1. Comparing **Figures 4A, 5A**, we observe up to 9 dB degradation in magnitude (for $d_{\mathrm{LOS}} = 1,750$ m and $d_1 = 250$ m), which corresponds to a power variation of 18 dB. In other words, it is possible to enable up to 18 dB variation in the received signal power by deliberately co-phasing and out-phasing the multipath components in the considered setup. It is worth noting that the normalized Doppler spectrum in **Figure 5B** is the same as that of **Figure 4B**.

As another extreme application of an RIS, the Doppler spread can be increased by intentionally increasing the Doppler shift of the reflected signal by $\theta(t) = 2\pi(\tilde{f}_D - f_D)t$ (mod 2π), where $\tilde{f}_D$ is the desired Doppler shift for the reflected signal. Here, a maximum desired Doppler shift of $0.5f_s$ Hz can be observed in simulation, where f_s is the sampling frequency for the continuous-wave signal. In **Figure 6**, we present the magnitude

of the complex envelope as well as the Doppler spectrum for the case of $d_{\mathrm{LOS}} = 1,500$ m and $d_1 = 500$ m by carefully adjusting the reflection phase to increase the Doppler spread (reduce the coherence time) by $\tilde{f}_D = 200$ and 400 Hz. As seen from **Figure 6**, an RIS can create new components in the Doppler spectrum, which results in a faster fade pattern for the complex envelope.

Going one step further, we consider the concept of random phase shifts by the RIS, in which the reflection phase is selected at random between 0 and 2π in each time interval. We illustrate the magnitude of the complex envelope and the Doppler spectrum in **Figure 7** for the case random reflection phases, where the reflection phase is selected at random in each sampling time for $d_{\mathrm{LOS}} = 1,500$ m and $d_1 = 500$ m. As seen from **Figures 7A,B**, although the effect in Doppler spectrum is not very significant, it would be possible to obtain a very fast fade pattern in time. Specifically, around 5 dB magnitude variations are observed within a sampling distance of $\lambda/32$ m. It would be possible to obtain an ultra-fast fade pattern by alternating the reflection phase between $\theta(t) = -4\pi f_D t + \pi$ (mod 2π) and $\theta(t) = -4\pi f_D t$ (mod 2π) in each time interval and this is left for interested readers.

3. ELIMINATING DOPPLER EFFECTS THROUGH INTELLIGENT REFLECTION

In this section, we focus on a simple scenario in which the direct link is blocked by an obstacle while the communication between
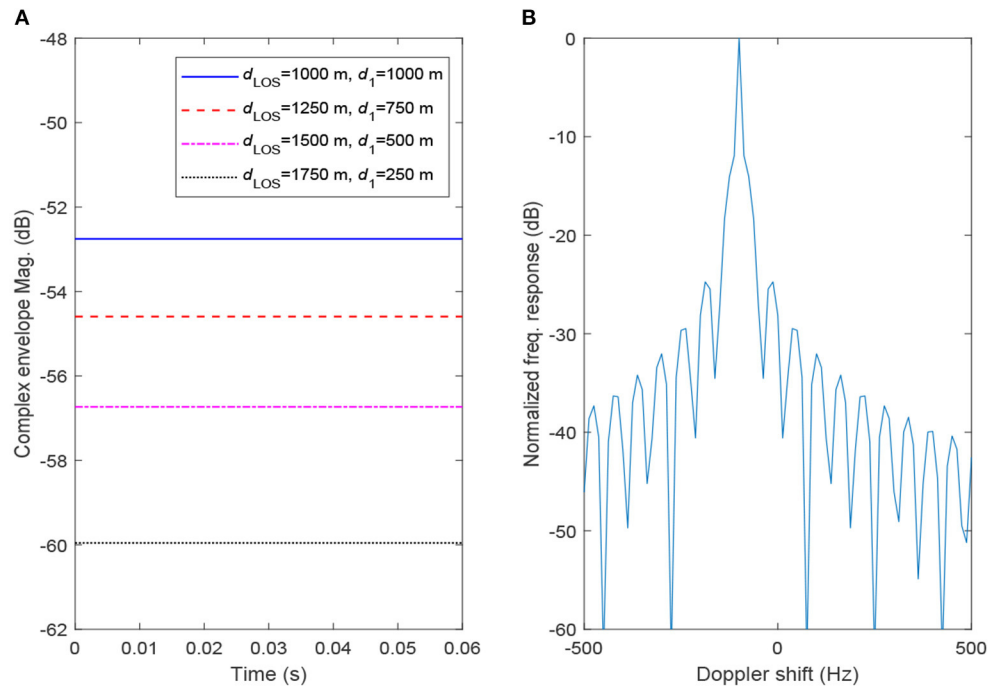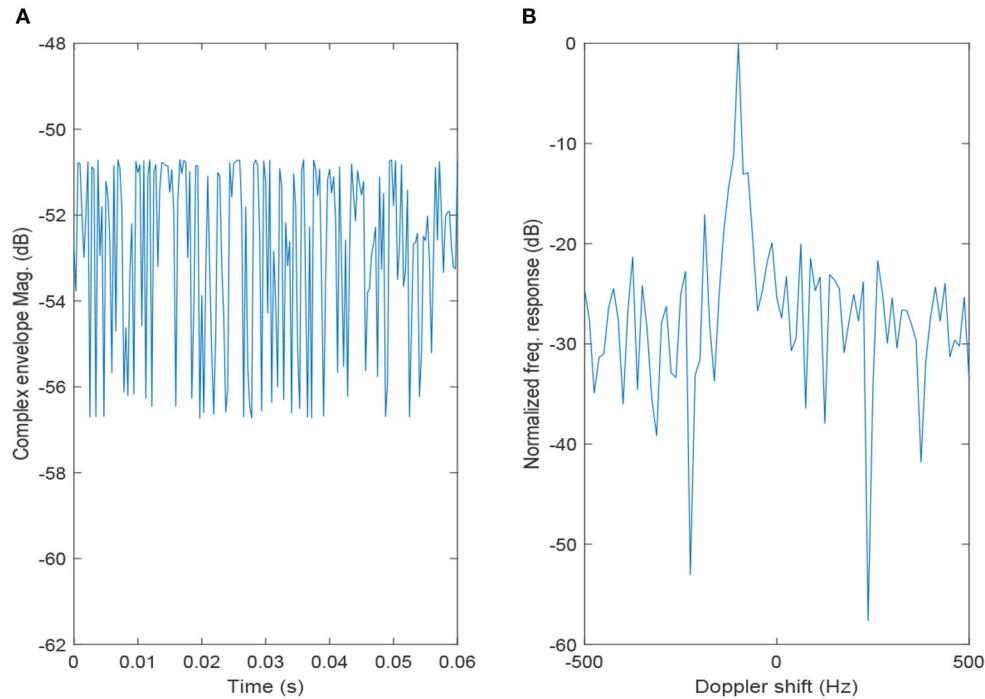
FIGURE 5 | (A) Minimized magnitude of the received signal in the presence of an RIS, **(B)** Doppler spectrum of the received signal for all scenarios.
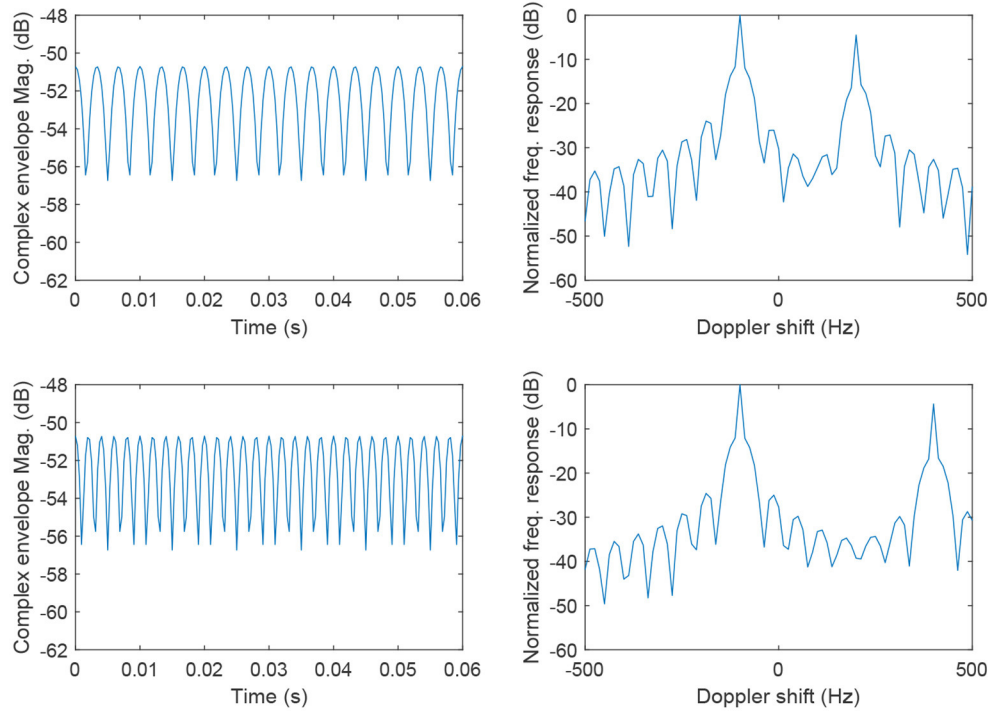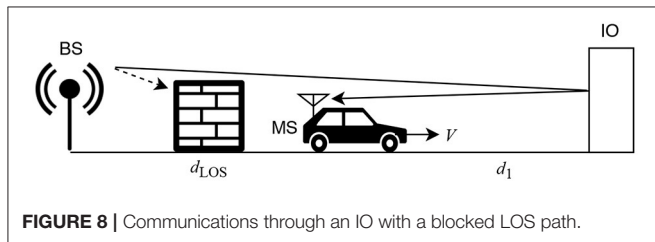

FIGURE 6 | Time varying magnitude and the Doppler spectrum of the received signal with increased Doppler effect for (Top) $\tilde{f}_D = 200$ Hz and (Bottom) $\tilde{f}_D = 400$ Hz.

FIGURE 7 | (A) Magnitude of the received signal in the presence of an RIS with random phases, **(B)** Doppler spectrum of the received signal.

FIGURE 8 | Communications through an IO with a blocked LOS path.

the BS and the MS is established through a reflection from an IO as shown in **Figure 8**. We consider the same assumptions of section II and investigate the Doppler effect on the received signal in the following two cases.

3.1. NLOS Transmission Without an RIS

Under the assumption of specular reflections from the IO with a reflection coefficient of $R = -1$, the received signal can be expressed as

$$r(t) = -\frac{\lambda}{4\pi} \frac{e^{-j\frac{2\pi d_R(t)}{\lambda}}}{d_R(t)} \tag{9}$$

where $d_R(t) = d_{\text{LOS}} + 2d_1 - Vt$ is the time-varying radio path distance for a MS moving with a speed of V m/s. Ignoring the constant phase terms and assuming a very short travel distance, the received signal can be expressed as

$$r(t) = -\frac{\lambda e^{j2\pi f_D t}}{4\pi (d_{\text{LOS}} + 2d_1)}. \tag{10}$$

As seen from (10), since only a single reflection occurs without a LOS signal and other multipath components, the received signal magnitude does not exhibit a fade pattern, that is, fixed with respect to time and given by $|r(t)| = \lambda/(4\pi (d_{\text{LOS}} + d_1))$. However, the received signal is still subject to a Doppler frequency shift of f_D Hz, which is evident from (10), due to the movement of the MS.

3.2. NLOS Transmission With an RIS

Here, we focus on the scenario of **Figure 8** while assuming that the IO is equipped with an RIS that is able to provide adjustable phase shifts, i.e., $R(t) = e^{j\theta(t)}$, as in section II. In this case, the received signal can be expressed as

$$r(t) = \frac{\lambda e^{j2\pi f_D t + j\theta(t)}}{4\pi (d_{\text{LOS}} + 2d_1)}. \tag{11}$$

As seen from (11), the magnitude of the received signal is independent from the reflection phase and the same as the previous case (without an RIS). However, it might be possible to completely eliminate the Doppler effect by adjusting the RIS reflection phase as $\theta(t) = -2\pi f_D t \pmod{2\pi}$. We give the following remark.

Remark 4: When there is no direct transmission between the BS and the MS over which the RIS has no control, intelligent reflection allows one to completely eliminate the Doppler effect,
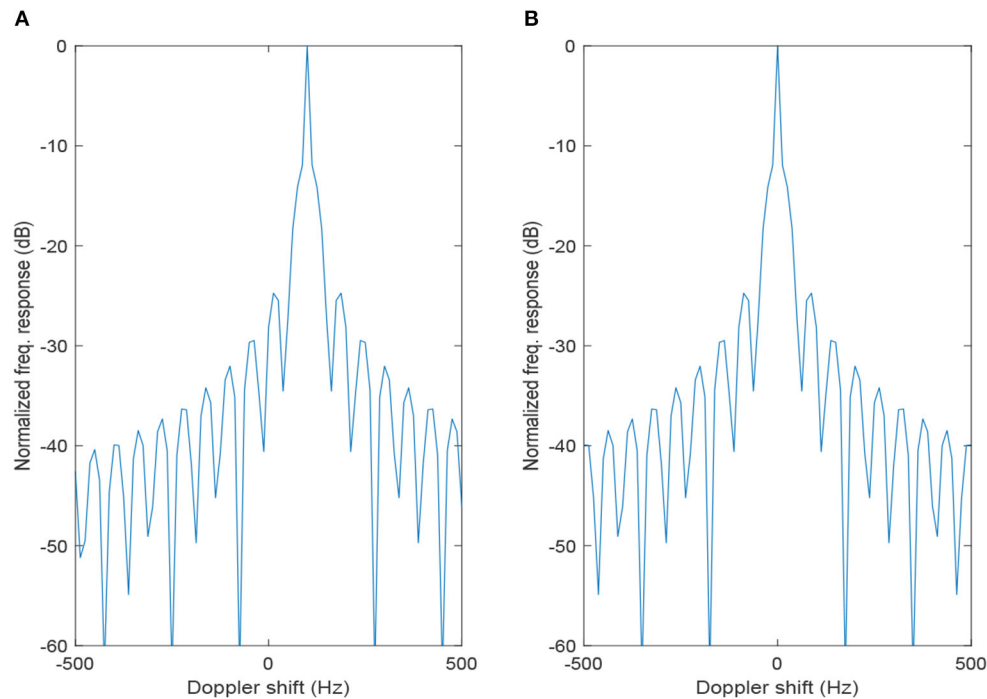
FIGURE 9 | Doppler spectrum of the received signal for the scenario of **Figure 8**: **(A)** without an RIS, **(B)** with an RIS.

TABLE 1 | Comparison of different RIS application scenarios.

Scenario	Figure #	Multipath mitigation	Doppler mitigation	Constant envelope
LOS + RIS	1	Yes	No	Yes
NLOS + RIS	8	n/a	Yes	Yes
LOS + RIS + IO	S1	Yes	No	No
LOS + 2 RISs	S1	Yes	No	Yes
NLOS + 2 RISs	n/a	Yes	Yes	Yes
LOS + N RISs + M IOs	S6	Yes	No	Yes (approx.)
NLOS + N RISs + M IOs	n/a	Yes	Yes (approx.)	Yes (approx.)

by carefully compensating the Doppler phase shifts through the RIS.

In **Figure 9**, we show the Doppler spectrum of the received signal with and without an RIS for $d_{\text{LOS}} = d_1 = 1,000$ m. As seen from **Figure 9**, the Doppler effect is eliminated (0 Hz) by adjusting the RIS reflections accordingly.

As discussed earlier, it is not possible the modify the magnitude of the complex envelope with an RIS for the scenario of **Figure 8**, however, as done in section II, the Doppler spread can be enhanced by $\theta(t) = 2\pi(\tilde{f}_D - f_D)t \pmod{2\pi}$, where $\tilde{f}_D$ is the desired Doppler frequency. The observation of the resulting spectrum is straightforward and left for the interested readers.

4. CONCLUSIONS AND FUTURE WORK

In this paper, we have revisited the multipath fading phenomenon of mobile communications and provided unique solutions by utilizing the emerging concept of RISs in the presence of Doppler effects. By following a bottom-up approach, first, we have investigated simple propagation scenarios with a single RIS and/or a plain IO. Then we have developed several novel methods for the case of multiple RISs and plain IOs depending on the their total numbers as well as the presence of the LOS path. Finally, we have considered a number of practical issues, including erroneous estimation of Doppler shifts, practical reflection phases, and discrete-time reflection phases, for the target setups and evaluated the overall performance under these imperfections. In **Table 1**, we summarize the main insights derived in this work for different RIS application scenarios.

One of the most important conclusions of this paper is that the multipath fading effect caused by the movement of the mobile receiver/transmitter can be effectively eliminated and/or mitigated by real-time tunable RISs. A number of interesting trade-offs have been demonstrated between fade pattern elimination and complex envelope magnitude maximization. While this work sheds light on the development of RIS-assisted mobile networks, exploration of amplitude/phase modulations and more practical path loss/propagation models appear as interesting future research directions.

DATA AVAILABILITY STATEMENT

The original contributions presented in the study are included in the article/**Supplementary Material**, further inquiries can be directed to the corresponding author/s.

AUTHOR CONTRIBUTIONS

The author confirms being the sole contributor of this work and has approved it for publication.

SUPPLEMENTARY MATERIAL

The Supplementary Material for this article can be found online at: https://www.frontiersin.org/articles/10.3389/frcmn.2021.672857/full#supplementary-material

REFERENCES

Abeywickrama, S., Zhang, R., and Yuen, C. (2020). "Intelligent reflecting surface: practical phase shift model and beamforming optimization," in *Proceedings of IEEE International Conference on Communications (ICC)*. doi: 10.1109/ICC40277.2020.9148961

Badiu, M. A., and Coon, J. P. (2020). Communication through a large reflecting surface with phase errors. *IEEE Wireless Commun. Lett.* 9, 184–188. doi: 10.1109/LWC.2019.2947445

Basar, E. (2016). Index modulation techniques for 5G wireless networks. *IEEE Commun. Mag.* 54, 168–175. doi: 10.1109/MCOM.2016.7509396

Basar, E. (2019a). Media-based modulation for future wireless systems: a tutorial. *IEEE Wireless Commun.* 26, 160–166. doi: 10.1109/MWC.2019.1800568

Basar, E. (2019b). "Transmission through large intelligent surfaces: a new frontier in wireless communications," in *Proceedings of European Conference on Networks and Communications (EuCNC 2019)* (Valencia). doi: 10.1109/EuCNC.2019.8801961

Basar, E. (2020). "Beyond massive MIMO: reconfigurable intelligent surface-assisted wireless communications," in *Flexible and Cognitive Radio Access Technologies for 5G and Beyond, Chapter 10*, eds H. Arslan and E. Basar (Stevenage Herts: IET), 317–338. doi: 10.1049/PBTE092E_ch10

Basar, E., Renzo, M. D., de Rosny, J., Debbah, M., Alouini, M. S., and Zhang, R. (2019). Wireless communications through reconfigurable intelligent surfaces. *IEEE Access* 7, 116753–116773. doi: 10.1109/ACCESS.2019.2935192

Basar, E., Wen, M., Mesleh, R., Renzo, M. D., Xiao, Y., and Haas, H. (2017). Index modulation techniques for next-generation wireless networks. *IEEE Access* 5, 16693–16746. doi: 10.1109/ACCESS.2017.2737528

Basar, E., and Yildirim, I. (2020a). Indoor and Outdoor Physical Channel Modeling and Efficient Positioning for Reconfigurable Intelligent Surfaces in mmWave Bands. *arXiv* [Under review]. Available online at: https://arxiv.org/abs/2006.02240

Basar, E., and Yildirim, I. (2020b). "SimRIS channel simulator for reconfigurable intelligent surface-empowered communication systems," in *Proceedings of IEEE Latin-American Conference on Communications*. doi: 10.1109/LATINCOM50620.2020.9282349

Basar, E., and Yildirim, I. (2020c). Reconfigurable intelligent surfaces for future wireless networks: a channel modeling perspective. *IEEE Wireless Commun.* 1–7. doi: 10.1109/MWC.001.2000338

Chen, J., Liang, Y. C., Pei, Y., and Guo, H. (2019). Intelligent reflecting surface: a programmable wireless environment for physical layer security. *IEEE Access* 7, 82599–82612. doi: 10.1109/ACCESS.2019.2924034

Cui, M., Zhang, G., and Zhang, R. (2019). Secure wireless communication via intelligent reflecting surface. *IEEE Wireless Commun. Lett.* 8, 1410–1414. doi: 10.1109/LWC.2019.2919685

Cui, T. J., Qi, M. Q., Wan, X., Zhao, J., and Cheng, Q. (2014). Coding metamaterials, digital metamaterials and programmable metamaterials. *Light Sci. Appl.* 3:e218. doi: 10.1038/lsa.2014.99

Dai, J. Y., Tang, W., Chen, M. Z., Chan, C. H., Cheng, Q., Jin, S., et al. (2021). Wireless communication based on information metasurfaces. *IEEE Trans. Microwave Theor. Tech.* 69, 1493–1510. doi: 10.1109/TMTT.2021.3054662

Dai, L., Wang, B., Wang, M., Yang, X., Tan, J., Bi, S., et al. (2020). Reconfigurable intelligent surface-based wireless communications: antenna design, prototyping, and experimental results. *IEEE Access* 8, 45913–45923. doi: 10.1109/ACCESS.2020.2977772

Danufane, F. H., Di Renzo, M., de Rosny, J., and Tretyakov, S. (2020). On the Path-Loss of Reconfigurable Intelligent Surfaces: An Approach Based on Green's Theorem Applied to Vector Fields. *arXiv* [Under review].

Di Renzo, M. (2019). Smart radio environments empowered by reconfigurable AI meta-surfaces: an idea whose time has come. *EURASIP J. Wireless Commun. Net.* 2019:129. doi: 10.1186/s13638-019-1438-9

Di Renzo, M., Zappone, A., Debbah, M., Alouini, M. S., Yuen, C., de Rosny, J., et al. (2020). Smart radio environments empowered by reconfigurable intelligent surfaces: How it works, state of research, and the road ahead. *IEEE J. Select. Areas Commun.* 38, 2450–2525. doi: 10.1109/JSAC.2020.3007211

Ding, Y., Kim, K. J., Koike-Akino, T., Pajovic, M., Wang, P., and Orlik, P. (2017). Spatial scattering modulation for uplink millimeter-wave systems. *IEEE Commun. Lett.* 21, 1493–1496. doi: 10.1109/LCOMM.2017.2684126

Ding, Z., and Poor, H. V. (2019). A simple design of IRS-NOMA transmission. *IEEE Commun. Lett.* 24, 1119–1123. doi: 10.1109/LCOMM.2020.2974196

Ellingson, S. (2019). Path Loss in Reconfigurable Intelligent Surface-Enabled Channels. *arXiv* [Under review].

Fontan, F. P., and Espineira, P. M. (2008). *Modeling the Wireless Propagation Channel: A Simulation Approach with MATLAB*. West Sussex: Wiley.

Fu, M., Zhou, Y., and Shi, Y. (2019). "Intelligent reflecting surface for downlink non-orthogonal multiple access networks," in *2019 IEEE Globecom Workshops (GC Wkshps)* (Waikoloa, HI). doi: 10.1109/GCWkshps45667.2019.9024675

Gatherer, A. (2018). *What Will 6G Be?* Available online at: https://www.comsoc.org/publications/ctn/what-will-6g-be

He, Z. Q., and Yuan, X. (2020). Cascaded channel estimation for large intelligent metasurface assisted massive MIMO. *IEEE Wireless Commun. Lett.* 9, 210–214. doi: 10.1109/LWC.2019.2948632

Huang, C., Alexandropoulos, G. C., Zappone, A., Debbah, M., and Yuen, C. (2018a). "Energy efficient multi-user MISO communication using low resolution large intelligent surfaces," in *Proceedings of IEEE Global Communications Conference* (Abu Dhabi). doi: 10.1109/GLOCOMW.2018.8644519

Huang, C., Zappone, A., Alexandropoulos, G. C., Debbah, M., and Yuen, C. (2019). Reconfigurable intelligent surfaces for energy efficiency in wireless communication. *IEEE Trans. Wireless Commun.* 18, 4157–4170. doi: 10.1109/TWC.2019.2922609

Huang, C., Zappone, A., Debbah, M., and Yuen, C. (2018b). "Achievable rate maximization by passive intelligent mirrors," in *Proceedings of 2018 IEEE International Conference on Acoustics, Speech and Signal Processing (ICASSP)* (Calgary, AB), 3714–3718. doi: 10.1109/ICASSP.2018.8461496

Kaina, N., Dupré, M., Lerosey, G., and Fink, M. (2014). Shaping complex microwave fields in reverberating media with binary tunable metasurfaces. *Sci. Rep.* 4:6693. doi: 10.1038/srep06693

Khandani, A. K. (2013). "Media-based modulation: a new approach to wireless transmission," in *Proceedings of IEEE International Symposium on Information Theory* (Istanbul), 3050–3054. doi: 10.1109/ISIT.2013.6620786

Liaskos, C., Nie, S., Tsioliaridou, A., Pitsillides, A., Ioannidis, S., and Akyildiz, I. (2018). A new wireless communication paradigm through software-controlled metasurfaces. *IEEE Commun. Mag.* 56, 162–169. doi: 10.1109/MCOM.2018.1700659

Liu, F., Tsilipakos, O., Pitilakis, A., Tasolamprou, A. C., Mirmoosa, M. S., Kantartzis, N. V., et al. (2019). Intelligent metasurfaces with continuously tunable local surface impedance for multiple reconfigurable functions. *Phys. Rev. Appl.* 11:044024. doi: 10.1103/PhysRevApplied.11.044024

Mishra, D., and Johansson, H. (2019). "Channel estimation and low-complexity beamforming design for passive intelligent surface assisted MISO wireless energy transfer," in *Proceedings of 2019 IEEE International Conference on Acoustics, Speech and Signal Processing (ICASSP)* (Brighton). doi: 10.1109/ICASSP.2019.8683663

Molisch, A. F. (2011). *Wireless Communications.* West Sussex, UK: Wiley.

Nadeem, Q. U. A., Kammoun, A., Chaaban, A., Debbah, M., and Alouini, M. S. (2020). Asymptotic max-min SINR analysis of reconfigurable intelligent surface assisted MISO systems. *IEEE Trans. Wireless Commun.* 19, 7748–7764. doi: 10.1109/TWC.2020.2986438

Saad, W., Bennis, M., and Chen, M. (2020). A vision of 6G wireless systems: applications, trends, technologies, and open research problems. *IEEE Netw.* 34, 134–142. doi: 10.1109/MNET.001.1900287

Subrt, L., and Pechac, P. (2012a). "Controlling propagation environments using intelligent walls," in *Proceedings of 2012 6th European Conference on Antennas and Propagation (EUCAP)* (Prague), 1–5. doi: 10.1109/EuCAP.2012.6206517

Subrt, L., and Pechac, P. (2012b). Intelligent walls as autonomous parts of smart indoor environments. *IET Commun.* 6, 1004–1010. doi: 10.1049/iet-com.2010.0544

Taha, A., Alrabeiah, M., and Alkhateeb, A. (2021). Enabling large intelligent surfaceswith compressive sensing and deep learning. *IEEE Access* 9, 44304–44321.

Tan, X., Sun, Z., Jornet, J. M., and Pados, D. (2016). "Increasing indoor spectrum sharing capacity using smart reflect-array," in *Proceedings of 2016 IEEE International Conference on Commununications (ICC)* (Kuala Lumpur), 1–6. doi: 10.1109/ICC.2016.7510962

Tan, X., Sun, Z., Koutsonikolas, D., and Jornet, J. M. (2018). "Enabling indoor mobile millimeter-wave networks based on smart reflect-arrays," in *Proceedings of IEEE Conference on Computer Communications (INFOCOM)* (Honolulu, HI), 270–278. doi: 10.1109/INFOCOM.2018.8485924

Tang, W. (2019). Wireless Communications with reconfigurable intelligent surface: path loss modeling and experimental measurement. *IEEE Trans. Wireless Commun.* 20, 421–439. doi: 10.1109/TWC.2020.3024887

Wu, Q., and Zhang, R. (2018). "Intelligent reflecting surface enhanced wireless network: joint active and passive beamforming design," in *Proceedings of IEEE Global Communication Conference* (Abu Dhabi). doi: 10.1109/GLOCOM.2018.8647620

Wu, Q., and Zhang, R. (2019a). "Beamforming optimization for intelligent reflecting surface with discrete phase shifts," in *Proceedings of 2019 IEEE International Conference on Acoustics, Speech and Signal Processing (ICASSP)* (Brighton). doi: 10.1109/ICASSP.2019.8683145

Wu, Q., and Zhang, R. (2019b). Towards smart and reconfigurable environment: intelligent reflecting surface aided wireless network. *IEEE Commun. Mag.* 58, 106–112. doi: 10.1109/MCOM.001.1900107

Wu, Q., Zhang, S., Zheng, B., You, C., and Zhang, R. (2020). Intelligent reflecting surface aided wireless communications: a tutorial. *IEEE Trans. Commun.* doi: 10.1109/TCOMM.2021.3051897

Xiong, X., Chan, J., Yu, E., Kumari, N., Sani, A. A., Zheng, C., et al. (2017). "Customizing indoor wireless coverage via 3D-fabricated reflectors," in *Proceedings of 4th ACM International Conference on Systems for Energy-Efficient Built Environments* (Delft), 1–10. doi: 10.1145/3137133.3137148

Yang, H., Cao, X., Yang, F., Gao, J., Xu, S., Li, M., et al. (2016). A programmable metasurface with dynamic polarization, scattering and focusing control. *Sci. Rep.* 6:35692. doi: 10.1038/srep35692

Yildirim, I., Uyrus, A., and Basar, E. (2020). Modeling and analysis of reconfigurable intelligent surfaces for indoor and outdoor applications in future wireless networks. *IEEE Trans. Commun.* 69, 1290–1301. doi: 10.1109/TCOMM.2020.3035391

Yu, X., Xu, D., and Schober, R. (2019a). "Enabling secure wireless communications via intelligent reflecting surfaces," in *Proceedings of IEEE Global Communication Conference (GLOBECOM)* (Waikoloa, HI). doi: 10.1109/GLOBECOM38437.2019.9014322

Yu, X., Xu, D., and Schober, R. (2019b). "MISO wireless communication systems via intelligent reflecting surfaces," in *2019 IEEE/CIC International Conference on Communications China (ICCC)* (Changchun). doi: 10.1109/ICCChina.2019.8855810

Supplementary Material

In this Supplementary Material, we investigate more sophisticated networks with multiple RISs and IOs as well as practical issues.

1 DOPPLER AND MULTIPATH FADING EFFECTS: CASE STUDIES WITH MULTIPLE REFLECTORS

In this supplementary section, we extend our system models and analyses in sections 2 and 3 into propagation scenarios with multiple IOs with and without intelligent reflection capabilities. We follow a bottom-up approach starting with two IOs and illustrate the fading/Doppler effect mitigation capabilities of RISs. We also propose a number of effective and novel methods with different functionalities.

1.1 Direct Signal and Two Reflected Signals without any RISs

In this subsection, by extending our model given in section 2, we consider the propagation scenario of **Figure S1** with two IOs. Here, in order to spice up our analyses, we assume that while the BS-MS and BS-IO 1-MS links are parallel to the ground, the reflected signal from IO 2 arrives to the MS with an angle of α with respect to the MS route. In this scenario, the initial (horizontal) distances between the BS and the MS, the MS and IO 1, and the MS and IO 2 are shown by d_{LOS}, d_1, and d_2, respectively. Using a similar analysis as in section 2, under the assumption of unit gain reflection coefficients for both IOs, that is $R_1 = R_2 = -1$, the time-varying received complex envelope can be expressed as

$$r(t) = \frac{\lambda}{4\pi} \left(\frac{e^{-j2\pi f_D t}}{d_{\text{LOS}}} - \frac{e^{j2\pi f_D t}}{d_{\text{LOS}} + 2d_1} - \frac{e^{j2\pi f_D (\cos\alpha)t - j\phi_2}}{\tilde{d}_2} \right) \tag{S1}$$

where $\tilde{d}_2 = \sqrt{d_2^2 \tan^2\alpha + (d_{\text{LOS}} + d_2)^2} + d_2/(\cos\alpha)$ is the initial radio path distance for the reflected signal of IO 2, which is obtained after simple trigonometric operations, and $\phi_2 = 2\pi\tilde{d}_2/\lambda$ is a fixed phase term. Here, we assume that the variations in terms of the large-scale path loss due to the movement of MS are almost negligible (as in **Figure 1**) and the rays from IO 2 remain parallel for all points of the mobile route, which corresponds to radio path distance decrements of $Vt\cos\alpha$, with respect to time, for these rays. It is worth noting that parallel ray assumption is approximately true for short route lengths (Goldsmith, 2005). As seen from (S1), the received signal has three Doppler components: $-f_D$ Hz, f_D Hz, and $f_D \cos\alpha$ Hz due to the rays coming from the BS, IO 1, and IO 2, respectively.

In **Figure S2**, we show the magnitude of the complex envelope as well as the Doppler spectrum for the case of $\alpha = 60°$, $d_{\text{LOS}} = d_1 = 1000$ m, and $d_2 = 500$ m. As seen from **Figure S2**, due to constructive and destructive interference of the direct and two reflected signals with different Doppler frequency shifts (-100 Hz, 100 Hz, and 50 Hz), the magnitude of the complex envelope exhibits a more hostile and faster fading pattern compared to the simpler scenario of **Figure 1** (see *Figure 2*, top-left subplot).

1.2 Direct Signal and Two Reflected Signals with One or Two RISs

In this subsection, we again focus on the scenario of **Figure S1**, however, under the assumption of one or two RISs that are attached to the existing IOs. Although being more challenging in terms of system

optimization and analysis, we focus on the case of a single RIS first, then extend our analysis into the case of two RISs.

1.2.1 One RIS

Let us assume that we have a single RIS that is mounted on the facade of IO 1 for the scenario of **Figure S1**. For this case, the received complex envelope can be expressed as

$$r(t) = \frac{\lambda}{4\pi} \left(\frac{e^{-j2\pi f_D t}}{d_{\text{LOS}}} + \frac{e^{j2\pi f_D t + j\theta_1(t)}}{d_{\text{LOS}} + 2d_1} - \frac{e^{j2\pi f_D(\cos\alpha)t - j\phi_2}}{\tilde{d}_2} \right). \tag{S2}$$

Here, we assumed that the intelligent reflection from IO 1 is characterized by $\theta_1(t)$. We investigate the following three methods for the adjustment of $\theta_1(t)$, where the corresponding complex envelope magnitudes and Doppler spectrums are shown in **Figure S3** for $\alpha = 60°$, $d_{\text{LOS}} = d_1 = 1000$ m, and $d_2 = 500$ m:

- Method 1: $\theta_1(t) = -4\pi f_D t \pmod{2\pi}$
- Method 2: $\theta_1(t) = 2\pi f_D t(\cos\alpha - 1) - \phi_2 + \pi \pmod{2\pi}$
- Method 3: $\theta_1(t) = 2\pi f_D t(\cos\alpha - 1) - \phi_2 \pmod{2\pi}$

In the first method, we intuitively align the reflected signal from the RIS to the LOS signal. As seen from **Figure S3**, although this adjustment eliminates the 100 Hz component in the spectrum and reduces the Doppler spread compared to the case without RIS (**Figure S2**), we still observe two components in the spectrum and a noticeable fade pattern for the received signal due to uncontrollable reflection through IO 2. It is worth noting that this might be the preferred option to obtain a high time average for the complex envelope magnitude with the price of a high Doppler spread (faster time variation).

In the second method, we align the reflected signal from the RIS to the one from IO 2, however, this worsens the situation by increasing the relative power of the 50 Hz component in the Doppler spectrum. As seen from **Figure S3**, a more severe fade pattern is observed for Method 2 due to destructive interference of the reflected signals to the LOS signal. This would be a preferred option in case of an eavesdropper to degrade its signal quality.

In the third method, we follow a clever approach and instead of aligning our RIS-assisted reflected signal to the existing two signals, we target to eliminate the uncontrollable reflection from IO 2 by out-phasing the reflected two signals. This results a remarkable improvement in both Doppler spectrum and the received complex envelope by almost mitigating the fade pattern. In other words, the RIS scarifies itself in Method 3 to eliminate the uncontrollable reflection from IO 2, which significantly reduces the multipath effect, while a minor variation is still observed due to different radio path lengths of these two signals. More specifically, for the selection of $\theta_1(t)$ in Method 3, we obtain

$$r(t) = \frac{\lambda}{4\pi} \left(\frac{e^{-j2\pi f_D t}}{d_{\text{LOS}}} + e^{j2\pi f_D(\cos\alpha)t - j\phi_2} \left(\frac{1}{d_{\text{LOS}} + 2d_1} - \frac{1}{\tilde{d}_2} \right) \right) \tag{S3}$$

which contains two components. However, the Doppler spread can be remarkably reduced when the radio path distances of the signals reflected from IO 1 and 2, i.e., $d_{\text{LOS}} + 2d_1$ and $\tilde{d}_2$, are close to each other. For instance, for the considered system parameters of d_{LOS}, d_1, d_2, and α in **Figure S3**, we have $\frac{1}{d_{\text{LOS}}} \gg \left(\frac{1}{d_{\text{LOS}} + 2d_1} - \frac{1}{\tilde{d}_2} \right)$, which results almost a single-tone received signal $r(t) \approx \frac{\lambda}{4\pi} \left(\frac{e^{-j2\pi f_D t}}{d_{\text{LOS}}} \right)$. This is also evident from the Doppler spectrum of the received signal for Method 3. However, Method 3 cannot guarantee the highest complex envelope magnitude, which is also observed from **Figure S3**.

To gain further insights, in **Figure S4**, we plot the 3D magnitude of the complex envelope with respect to time and varying $\theta_1(t)$ values between 0 and 2π. As seen from **Figure S4**, due to constructive and destructive interference of multipath components (particularly due to the interference of the signal reflected from IO 2), the complex envelope exhibits several deep fades. We also observe that it is not feasible to fix the complex envelope magnitude to its maximum value (-48.69 dB for this specific setup) as in the case of single reflection since the incoming three signals cannot be fully aligned at all times. Finally, we note that performing an exhaustive search for the determination of the optimum reflection phase that maximizes $|r(t)|$ for each time sample might be possible with different system parameters, however, this does not fit within the scope of this study, which explores effective solutions for the RIS configuration. We also verify from **Figure S4** that Method 1 achieves approximately the maximum magnitude for the complex envelope in the considered experiment. In light of our discussion above, we give the following remark:

Remark 5: For the case of two reflections with a single RIS in **Figure S1**, the heuristic choice to maximize the magnitude of the complex envelope is to align the reflected signal to the stronger component, that is, the LOS signal (Method 1) under normal circumstances. While this ensures a very high magnitude for the complex envelope, we still observe a fade pattern in time domain. On the other hand, the RIS can be reversely aligned to the reflected signal from the plain IO (Method 3) to reduce the Doppler spread at the price of a slight degradation in the magnitude of the complex envelope.

Remark 6: For the setup of **Figure S1**, the optimal reflection phase that maximizes the magnitude of the complex envelope is given by

$$\theta_1(t) = \frac{\pi}{2}(1 - \text{sgn}(A)) - \tan^{-1}(-B/A) \tag{S4}$$

where $\text{sgn}(\cdot)$ is the sign function and

$$A = \frac{1}{d_{\text{LOS}}}\cos(4\pi f_D t) - \frac{1}{\tilde{d}_2}\cos(2\pi f_D(1 - \cos\alpha)t + \phi_2)$$
$$B = \frac{-1}{d_{\text{LOS}}}\sin(4\pi f_D t) + \frac{1}{\tilde{d}_2}\sin(2\pi f_D(1 - \cos\alpha)t + \phi_2). \tag{S5}$$

The proof of (S4) is given in Appendix. In **Figure S5**, we compare the reflection phases as well as magnitudes of the complex envelope for Method 1 and the optimum method for the same system parameters. As seen from **Figure S5**, Method 1 provides a very close phase behavior compared to the optimal one due to the stronger LOS path and a very minor degradation can be observed in the magnitude of the complex envelope. Nevertheless, the optimal reflection phase in (S4) is valid for all possible system parameters in **Figure S1** and guarantees the maximum complex envelope magnitude at all times. For reference, magnitude values are also shown in the same figure for Method 3. As seen from **Figure S5**, Method 3 reduces the severity of the fade pattern (Doppler spread) while ensuring the same minimum magnitude at the price of a lower time average for the complex envelope.

1.2.2 Two RISs

Under the assumption of two RISs attached to the existing two IOs in the system of **Figure S1**, the received complex envelope is obtained as

$$r(t) = \frac{\lambda}{4\pi} \left(\frac{e^{-j2\pi f_D t}}{d_{\text{LOS}}} + \frac{e^{j2\pi f_D t + j\theta_1(t)}}{d_{\text{LOS}} + 2d_1} + \frac{e^{j2\pi f_D(\cos\alpha)t - j\phi_2 + j\theta_2(t)}}{\tilde{d}_2} \right) \tag{S6}$$

where the time-varying and intelligent reflection characteristics of RIS 1 and 2 are captured by $\theta_1(t)$ and $\theta_2(t)$, respectively. Here, compared to the previous case, we have more freedom with two controllable reflections and the magnitude of the received signal can be maximized (and the Doppler spread can be minimized) by readily aligning the reflected signals to the LOS signal. This can be done by setting $\theta_1(t) = -4\pi f_D t \pmod{2\pi}$ and $\theta_2(t) = -2\pi f_D t(1 + \cos\alpha) + \phi_2 \pmod{2\pi}$, which results

$$r(t) = \frac{\lambda e^{-j2\pi f_D t}}{4\pi} \left(\frac{1}{d_{\text{LOS}}} + \frac{1}{d_{\text{LOS}} + 2d_1} + \frac{1}{\tilde{d}_2} \right). \tag{S7}$$

Similar to the case with single intelligent reflection (subsection 2.2), we obtain a constant-amplitude complex envelope and a minimized Doppler spread (with a single component at $-f_D$ Hz) due to the clever co-phasing of the multipath components. Interested readers may easily obtain the magnitude and the Doppler spectrum of the complex envelope to verify our findings.

1.3 Two RISs without a LOS path

Finally, we extend our analysis for the case of non-LOS transmission through two RISs, which yields

$$r(t) = \frac{\lambda}{4\pi} \left(\frac{e^{j2\pi f_D t + j\theta_1(t)}}{d_{\text{LOS}} + 2d_1} + \frac{e^{j2\pi f_D(\cos\alpha)t - j\phi_2 + j\theta_2(t)}}{\tilde{d}_2} \right). \tag{S8}$$

Similar to the case in section 3, by carefully adjusting the phases of two RISs, the Doppler effect can be totally eliminated due to the nonexistence of the LOS signal, which is out of control of the RISs. It is evident that this can be done by $\theta_1(t) = -2\pi f_D t \pmod{2\pi}$ and $\theta_2(t) = -2\pi f_D(\cos\alpha)t + \phi_2 \pmod{2\pi}$.

1.4 The General Case with Multiple IOs and the Direct Signal

Against this background, in this subsection, we extend our analyses for the general case of **Figure S6**, which consists of a total of R IOs. Here, we assume that N of them are coated with RISs, while the remaining $M = R - N$ ones are plain IOs, which create uncontrollable specular reflections towards the MS. In this scenario (N RISs and M plain IOs), the received complex envelope is given by

$$r(t) = \frac{\lambda}{4\pi} \left(\frac{e^{-j2\pi f_D t}}{d_{\text{LOS}}} + \sum_{i=1}^{N} \frac{e^{j2\pi f_{R,i}t - j\psi_i + j\theta_i(t)}}{\tilde{d}_{R,i}} - \sum_{k=1}^{M} \frac{e^{j2\pi f_{I,k}t - j\phi_k}}{\tilde{d}_{I,k}} \right). \tag{S9}$$

Here, we assume that all rays stemming from IOs remain parallel during the movement of the MS for a short period of time, which is a valid assumption, and without loss of generality, we consider a reflection coefficient of -1 for the plain IOs. Additionally, the corresponding terms in (S9) are defined as follows:

- $f_{R,i}$: Doppler shift for the ith RIS

- $f_{I,k}$: Doppler shift for the kth plain IO
- ψ_i: Constant phase shift for the ith RIS
- ϕ_k: Constant phase shift for the kth plain IO
- $\tilde{d}_{R,i}$: Initial radio path distance for the ith RIS
- $\tilde{d}_{I,k}$: Initial radio path distance for the kth plain IO
- $\theta_i(t)$: Adjustable phase shift of the ith RIS

Here, the Doppler shifts of the RISs and plain IOs are not only dependent on the speed of the MS, but also on their relative positions with respect to the MS, i.e., angles of arrival for the incoming signals: $f_{R,i} = f_D \cos \alpha_i$ and $f_{I,k} = f_D \cos \beta_k$, where α_i and β_k are the angles of arrival for the reflected signals of ith RIS and kth plain IO, respectively. In this generalized scenario, we focus on the following two setups:

1.4.1 Setup I ($N \leq M$)

In this setup, we have more number of uncontrollable reflectors (plain IOs) than RISs. Consequently, we extend our methods in Supplementary subsection 1.2 and target either directly aligning N RISs to the LOS path (to improve the received signal strength) or eliminating the reflections stemming from N out of M plain IOs (to reduce the Doppler spread). While the alignment of the reflected signals to the LOS signal is straightforward (Method 1), the assignment of N RISs to corresponding IOs in real-time appears as an interesting design problem. For this purpose, we consider a brute-force search algorithm to determine the most effective set of IOs to be targeted by RISs (Methods 2 & 3). More specifically, N out of M IOs can be selected in $C(M, N)$ different ways, where $C(\cdot, \cdot)$ is the binomial coefficient. Since these N RISs can be assigned to N plain IOs in $N!$ ways, we obtain a total of $P(M, N) = C(M, N)N!$ possibilities (permutations) for the assignment of N RISs to M IOs. Our methodology has been summarized below:

- Method 1: We align the existing N RISs to the LOS path by adjusting their reflection phases as $\theta_i(t) = -2\pi f_{R,i}t + \psi_i - 2\pi f_D t \pmod{2\pi}$ for $i = 1, 2, \ldots, N$.
- Method 2: For the ith RIS minimizing the effect of the reflection stemming from the kth IO, i.e., ith RIS out-phased with the kth plain IO, we have the following reflection phase: $\theta_i(t) = -2\pi f_{R,i}t + \psi_i + 2\pi f_{I,k}t - \phi_k \pmod{2\pi}$ for $i = 1, 2, \ldots, N$ and $k = 1, 2, \ldots, M$. Considering these given reflection phases, for each time instant, we search for all possible N-permutations of M plain IOs to maximize the absolute value of the complex envelope. Then, the permutation of IOs that maximizes the complex envelope magnitude is selected. This method requires a search over $P(M, N)$ permutations in each time instant, in return, has a higher complexity than the first one. Specifically, let us denote the nth permutation (the set of IOs) by $\mathcal{P}_n = \{\mathcal{P}_n^1, \mathcal{P}_n^2 \ldots, \mathcal{P}_n^N\}$ for $n = 1, 2, \ldots, P(M, N)$. For a given time instant $t = t_0$, considering all permutations, we construct the possible the set of RIS phases as $\theta_i(t_0) = -2\pi f_{R,i}t_0 + \psi_i + 2\pi f_{I,\mathcal{P}_n^i}t_0 - \phi_{\mathcal{P}_n^i} \pmod{2\pi}$ for $i = 1, 2, \ldots, N$ and the corresponding estimate of the received signal sample $r_n(t_0)$ is obtained from (S9) for the nth permutation. Finally, the optimum permutation is obtained as $\hat{n} = \arg\max_n |r_n(t_0)|$. Then, the optimal set of plain IOs to be targeted by RISs are determined as $\mathcal{P}_{\hat{n}}$ and the RIS reflection phases are adjusted accordingly: $\hat{\theta}_i(t_0) = -2\pi f_{R,i}t_0 + \psi_i + 2\pi f_{I,\mathcal{P}_{\hat{n}}^i}t_0 - \phi_{\mathcal{P}_{\hat{n}}^i} \pmod{2\pi}$ for $i = 1, 2, \ldots, N$. These procedures are repeated for all time instants. Obviously, this strategy requires the knowledge of all Doppler phases at a central processing unit, estimation of the received complex envelope samples, and a dynamic control of all RISs.
- Method 3: This method uses the same exhaustive search approach of Method 2, however, instead of maximizing the the absolute value of the complex envelope, we try to minimize the variation of it with respect to time by assigning the RISs to IOs with this purpose. Specifically, for a given time instant

$t = t_0$, the optimal permutation $\mathcal{P}_{\hat{n}}$ is obtained as $\hat{n} = \arg\min_n \big| |r_n(t_0)| - |r(t_{-1})| \big|$, where $r(t_{-1})$ is the sample of the received signal at the previous time instant, while at $t = 0$, we determine the optimal permutation as in Method 2. This method directly targets to eliminate fade patterns of the complex envelope instead of focusing on the maximization of the received signal strength by aligning (co-phasing) RISs with certain IOs. In other words, Method 3 eliminates the variations in the received signal stemming from different Doppler shifts of the incoming signals.

1.4.2   Setup II ($N > M$)

In this setup, we have more number of RISs than the plain IOs, and consequently, have much more freedom in the system design. Here, we consider the same three methods discussed above (Setup I) for the adjustment of RIS reflection phases, however, slight modifications are performed for Methods 2 and 3 due to fewer number of plain IOs in this setup. In Method 1, we align the existing RISs to the LOS path as in Setup I. To reduce the Doppler spread by Method 2, we search for all possible M-permutations of RISs to target plain IOs, i.e., a total of $P(N, M)$ permutations are considered. More specifically, at each time instant, we consider all possible RIS permutations to eliminate the reflections from M plain IOs, while the remaining $N - M$ RISs are aligned to the LOS path. The permutation of RISs that maximizes the absolute value of the sample of the received signal is selected. On the other hand, Method 3 aims to minimize the variations in $r(t)$ by assigning M RISs to M plain IOs, while also aligning the remaining $N - M$ RISs to the LOS path. Our methodology has been summarized as follows:

- Method 1: The same as Method 1 for Setup I.
- Method 2: Let us denote the nth permutation (the set of RISs) by $\mathcal{R}_n = \{\mathcal{R}_n^1, \mathcal{R}_n^2 \ldots, \mathcal{R}_n^M\}$ and the set of RISs that are not included in the nth permutation by $\mathcal{S}_n = \{\mathcal{S}_n^1, \mathcal{S}_n^2 \ldots, \mathcal{S}_n^{N-M}\}$, i.e., $\mathcal{P}_n \cup \mathcal{S}_n = \{1, 2, \ldots, N\}$ for $n = 1, 2, \ldots, P(N, M)$. For a given time instant $t = t_0$, considering all permutations, we construct the possible the set of RIS phases to eliminate IO reflections as $\theta_{\mathcal{R}_n^i}(t_0) = -2\pi f_{R,\mathcal{R}_n^i} t_0 + \psi_{\mathcal{R}_n^i} + 2\pi f_{I,i} t_0 - \phi_i \pmod{2\pi}$ for $i = 1, 2, \ldots, M$, while aligning the remaining $N - M$ RISs to the LOS path as follows: $\theta_{\mathcal{S}_n^i}(t_0) = -2\pi f_{R,\mathcal{S}_n^i} t_0 + \psi_{\mathcal{S}_n^i} - 2\pi f_D t_0 \pmod{2\pi}$ for $i = 1, 2, \ldots, N - M$. Then, the corresponding estimate of the received signal sample $r_n(t_0)$ is obtained from (S9) for the nth permutation. Finally, the optimum permutation is obtained as $\hat{n} = \arg\max_n |r_n(t_0)|$. Then, the optimal set of RISs to be paired with IOs and aligned to the LOS path are determined as $\mathcal{R}_{\hat{n}}$ and $\mathcal{S}_{\hat{n}}$, respectively, and the RIS reflection phases are adjusted accordingly: $\hat{\theta}_{\mathcal{R}_{\hat{n}}^i}(t_0) = -2\pi f_{R,\mathcal{R}_{\hat{n}}^i} t_0 + \psi_{\mathcal{R}_{\hat{n}}^i} + 2\pi f_{I,i} t_0 - \phi_i \pmod{2\pi}$ for $i = 1, 2, \ldots, M$ and $\hat{\theta}_{\mathcal{S}_{\hat{n}}^i}(t_0) = -2\pi f_{R,\mathcal{S}_{\hat{n}}^i} t_0 + \psi_{\mathcal{S}_{\hat{n}}^i} - 2\pi f_D t_0 \pmod{2\pi}$ for $i = M+1, M+2, \ldots, N$. The above procedures are repeated for all time samples.
- Method 3: This method follows the same procedures as that of Method 2, except the determination of the optimum permutation. This is performed by $\hat{n} = \arg\min_n \big| |r_n(t_0)| - |r(t_{-1})| \big|$ considering the current (estimated corresponding to the nth permutation) and previously received signal samples of $r_n(t_0)$ and $r(t_{-1})$.

To illustrate the potential of our methods, we consider the 2D geometry of **Figure S7** in our computer simulations, where the MS and the BS are located at $(0, 0)$ and $(-1000, 0)$ in terms of their (x, y)-coordinates, respectively. We assume that $R = 10$ IOs are uniformly distributed in a predefined rectangular area at the right hand side of the origin. We again consider a mobile speed of $V = 10$ m/s with $f_c = 3$ GHz and a sampling time of $\lambda/32$, but use the following new simulation parameters: a travel distance of $30\lambda = 3$ m and an FFT size of 1024.

Table S1. Comparison of Methods 1-3 in terms of peak-to-peak variation (Δ_r in dB) and time-average ($\bar{r}$ in dB) of $|r(t)|$.

	Method 1	Method 2	Method 3
$N = 3, M = 7$	$\Delta_r = 11.78$ $\bar{r} = -47.22$	$\Delta_r = 5.43$ $\bar{r} = -47.76$	$\Delta_r = 3.95$ $\bar{r} = -50.17$
$N = M = 5$	$\Delta_r = 7.08$ $\bar{r} = -45.99$	$\Delta_r = 3.09$ $\bar{r} = -49.93$	$\Delta_r = 2.47$ $\bar{r} = -50.88$
$N = 7, M = 3$	$\Delta_r = 2.91$ $\bar{r} = -44.90$	$\Delta_r = 1.05$ $\bar{r} = -46.20$	$\Delta_r = 0.66$ $\bar{r} = -46.62$

In **Figure S8**, we investigate two extreme cases: $N = 0, M = 10$ and $N = 10, M = 0$. For the case of $N = 0, M = 10$, i.e., the case without any RISs, we observe a Doppler spectrum consisting of many components and in return, a severe deep fading pattern in the time domain. On the contrary, for the case of $N = 10, M = 0$, in which all IOs in the system are equipped with RISs, we have a full control of the propagation environment by applying Method 1 (aligning the reflected signals from all RISs to the LOS path) and observe a constant magnitude for the complex envelope as in subsection 2.2. Here, we may readily state that the case of $N = 10, M = 0$ with Method 1 provides the maximum magnitude for the complex envelope and can be considered as a benchmark for all setups/methods with $M > 0$.

In **Figures S9-S11**, we consider three different scenarios based on the number of RISs in the system: $N = 3, M = 7$ (Setup I), $N = M = 5$ (Setup I), and $N = 7, M = 3$ (Setup II) and assess the potential of the introduced Methods 1-3. As seen from **Figures S9-S11**, although Method 1 ensures a high complex envelope magnitude in average with the price of a larger Doppler spread (faster variation in time), Methods 2 and 3 are more effective in reducing the fade patterns observed in the time domain by modifying the Doppler spectrum through the elimination of plain IO signals. Particularly, the improvements provided by Method 3 are more noticeable both in time and frequency domains. For instance, for the case of $N = 7, M = 3$, Method 3 almost eliminates all Doppler spectrum components stemming from three plain IOs and ensures an approximately constant magnitude for the complex envelope, as seen from **Figure S11**.

To gain further insights, in Table S1, we provide a quantitative analysis by comparing the peak-to-peak value Δ_r of $|r(t)|$ and its time average $\bar{r}$ (both measured in dB) for all methods, i.e., $\Delta_r = |r(t)|_{\max} - |r(t)|_{\min}$ and $\bar{r} = \frac{1}{n_s} \sum_{n=0}^{n_s-1} |r(it_s)|$, where n_s and t_s respectively stand for the total number of time samples and sampling time, which are selected as $n_s = 960$ and $t_s = 0.3125$ ms for this specific simulation. As observed from Table S1, increasing N noticeably reduces Δ_r for all methods, while this reduction is more remarkable for Methods 2 and 3. We also evince that Methods 2 and 3 cause in a slight degradation in $\bar{r}$ since they utilize RISs to cancel out reflections from plain IOs. Generalizing our discussion from Subsection 4.2.1, we claim that Method 1 can be the preferred choice to maximize the (time-averaged) magnitude of the complex envelope due to the stronger LOS path, however, the complete mathematical proof of this claim is highly intractable. We also observe that Method 2 provides a nice compromise between Methods 1 and 3 by providing a much lower Δ_r with a close $\bar{r}$ compared to Method 1, while Method 3 ensures the minimum Δ_r.

1.5 The General Case with Multiple IOs and without the Direct Signal

In this section, we revisit the general case of the previous section (**Figure S6**), however, without the presence of a LOS path. For this case, the received signal with N RISs and M plain IOs can be expressed as follows:

$$r(t) = \frac{\lambda}{4\pi} \left(\sum_{i=1}^{N} \frac{e^{j2\pi f_{R,i}t - j\psi_i + j\theta_i(t)}}{\tilde{d}_{R,i}} - \sum_{k=1}^{M} \frac{e^{j2\pi f_{I,k}t - j\phi_k}}{\tilde{d}_{I,k}} \right). \tag{S10}$$

Here, the three methods introduced in Supplementary subsection 1.4 can be applied with slight modifications. For Method 1, since there is no LOS path, the available RISs in the system can be aligned to the strongest path, which might be from either an RIS or a plain IO and has the shortest radio path distance. For Methods 2 and 3, when $M \geq N$, we use the same procedures as in the LOS case and assign all N RISs to the plain IOs with different purposes. However, when $N > M$, after applying the same permutation selection procedures, we determine the RIS with the strongest path among the remaining $N - M$ RISs in lieu of the LOS path and align the rest of the RISs ($N - M - 1$ ones) to this strongest RIS for each specific permutation. Our methodology has been summarized below:

1.5.1 Setup I ($M \geq N$)

- Method 1: We align the existing N RISs to the strongest path. If the strongest path belongs to a RIS, whose index is a, we have $\theta_i(t) = -2\pi f_{R,i}t + \psi_i + 2\pi f_{R,a}t - \psi_a \pmod{2\pi}$ for $i = 1, \ldots, a-1, a+1, \ldots, N$, while $\theta_a(t) = 0$. Otherwise, if the strongest path belongs to a plain IO with index a, we have $\theta_i(t) = -2\pi f_{R,i}t + \psi_i + 2\pi f_{I,a}t - \phi_a + \pi \pmod{2\pi}$ for $i = 1, 2, \ldots, N$. Please note that $a = \arg\min_i \tilde{d}_{R,i}$ if $\min_i \tilde{d}_{R,i} < \min_k \tilde{d}_{I,k}$ or $a = \arg\min_k \tilde{d}_{I,k}$, otherwise.
- Method 2: The same as Method 2 in Supplementary subsection 1.4 for $M \geq N$ except that $r_n(t_0)$ is obtained from (S10) for the nth permutation.
- Method 3: The same as Method 3 in Supplementary subsection 1.4 for $M \geq N$ except that $r_n(t_0)$ is obtained from (S10) for the nth permutation.

1.5.2 Setup II ($N > M$)

- Method 1: The same as Method 1 given above.
- Method 2: We follow the same steps for Method 2 in subsection 1.4 for $N > M$, however, for nth permutation, the strongest RIS is selected among the set $\mathcal{S}_n$ (the set of $N - M$ RISs that are not included in the elimination of IO reflections). Denoting the index of this strongest RIS by a_n, where $a_n = \arg\min_{i \in \mathcal{S}_n} \tilde{d}_{R,i}$, we have $\theta_{\mathcal{S}_n^i}(t_0) = -2\pi f_{R,\mathcal{S}_n^i}t_0 + \psi_{\mathcal{S}_n^i} + 2\pi f_{R,a_n}t_0 - \psi_{a_n} \pmod{2\pi}$ for $i = 1, 2, \ldots, N - M$ with $\mathcal{S}_n^i \neq a_n$ and $\theta_{a_n}(t_0) = 0$ for this case. The above procedures are repeated for all permutations and the estimates of the received signal samples are obtained as $r_n(t_0)$ from (S10) for $n = 1, 2, \ldots, P(N, M)$. After the determination of the optimal permutation $\hat{n}$, we obtain the set of RISs targeting the IOs as $\mathcal{R}_{\hat{n}}$ while the set of remaining RISs are given by $\mathcal{S}_{\hat{n}}$. Finally, RIS angles are determined as in Method 2 in subsection 1.4 for $N > M$ with the exception that the phases of the remaining $N - M$ RISs are aligned as $\hat{\theta}_{\mathcal{S}_{\hat{n}}^i}(t_0) = -2\pi f_{R,\mathcal{S}_{\hat{n}}^i}t_0 + \psi_{\mathcal{S}_{\hat{n}}^i} + 2\pi f_{R,a_{\hat{n}}}t_0 - \psi_{a_{\hat{n}}} \pmod{2\pi}$ for $i = 1, 2, \ldots, N - M$ with $\mathcal{S}_{\hat{n}}^i \neq a_{\hat{n}}$ and $\hat{\theta}_{a_{\hat{n}}}(t_0) = 0$. The above procedures are repeated for all time instants.
- Method 3: This method follows the same procedures as that of Method 2 given above, except the determination of the optimum permutation, which is discussed in Supplementary subsection 1.4.

In **Figures S12,S13**, we investigate the application of Methods 1-3 in two scenarios: $N = 3, M = 7$ (Setup I) and $N = 7, K = 3$ (Setup II) for the same simulation scenario of **Figure S7** by ignoring the LOS path. Compared to **Figures S9,S11**, we observe that due to the nonexistence of the LOS path, all methods

provide a similar level of time-average ($\bar{r}$) for the complex envelope while Methods 2 and 3 eliminate deep fades in the received signal. In other words, since we do not have a stronger LOS path, Method 1 loses its main advantage in terms of $\bar{r}$ compared to the other two methods for both scenarios.

It is worth noting that for the case of $N = 0$, none of the methods are applicable as in the case of the previous section. However, for $M = 0$, Doppler effect can be totally eliminated due to the nonexistence of the LOS path as follows: $\theta_i(t) = -2\pi f_{R,i}t + \phi_i \pmod{2\pi}$ for $i = 1, 2, \ldots, N$.

As a final note, our aim here is to find heuristic solutions to mitigate deep fading and Doppler effects under arbitrary number of RISs and plain IOs, and the determination of the ultimately optimum RIS angles are beyond the scope of this work. Although our methods provide satisfactory results, there might be a certain permutation of RISs/IOs with specific reflection phases that may guarantee a maximized received complex envelope magnitude and/or the lowest Doppler spread. However, the theoretical derivation of this ultimate optimal solution seems intractable at this moment.

2 PRACTICAL ISSUES

In this supplementary section, we consider a number of practical issues and investigate the performance of our solutions under certain imperfections in the system.

2.1 Realistic RISs

Throughout this paper, we assumed that the utilized RISs have a unit-amplitude reflection coefficient with a very high resolution reflection phase $\theta(t) \in [0, 2\pi)$ that can be tuned in real time. However, as reported in recent studies, there can be not only a dependency between the amplitude and the phase but also a limited range can be supported for the reflection phase. For this purpose, we consider the realistic RIS design of Tretyakov *et al.* (Liu et al., 2019), which has a reflection amplitude of -1 dB with a reflection phase between $-150°$ and $140°$. In **Figure S14**, we compare the complex envelope magnitudes of two scenarios in the presence of a perfect RIS (P-RIS) and an imperfect RIS (I-RIS) with practical constraints: i) the scenario of **Figure 1** with $N = 1, M = 0$ and ii) the scenario of **Figure S1** with $N = M = 1$. As seen from **Figure S14**, the practical RIS of (Liu et al., 2019) causes a slight degradation both in magnitude and shape of the complex envelope, however, its overall effect is not significant. A further degradation would be expected in the presence of discrete phase shifts (Wu and Zhang, 2019), and this analysis is left for interested readers.

2.2 Imperfect Knowledge of Doppler Frequencies

As discussed in Supplementary section 1, in case of multiple RISs, a central processing unit needs to acquire the knowledge of Doppler frequencies of all incoming rays to initiate Methods 1-3 in coordination with the available RISs. Here, we assume that due to erroneous estimation of the velocity of the MS and/or relative positions of the IOs, the RISs in the system are fed back with erroneous Doppler shifts (in Hz), given by $f_{R,i}^e = f_{R,i} + e_{R,i}$ and $f_{I,k}^e = f_{I,k} + e_{I,k}$, while the dominant Doppler shift (f_D) stemming from the LOS path is perfectly known. Here, $e_{R,i}$ and $e_{I,k}$ respectively stand for the errors in Doppler shifts for ith RIS and kth plain IO. To illustrate the effect of this imperfection, these estimation error terms are modelled by independent and identically distributed uniform random variables in the range $[-U, U]$ (in Hz). In **Figure S15**, we consider the scenario of $N = 7, M = 3$ with $U = 0, 1$ and 3 for the same geometry of **Figure S7**. As seen from **Figure S15**, while the degradation in the complex envelope is not a major concern for $U = 1$, a significant distortion has been observed for the case of $U = 4$ with respect to time. Here,

Methods 2 and 3 appear more reliable in the presence of Doppler frequency estimation errors, however, we observe that the overall system is highly sensitive to this type of error.

We note that the estimation of Doppler frequencies and/or real-time adaptation of RISs in realistic channel conditions are interesting research problems to be investigated with the framework of RIS-empowered systems.

2.3 High Mobility & Discrete-Time RIS Phases

In this subsection, we will focus on the case of high mobility under the assumption of discrete-time RIS reflection phases. In this scenario, the RIS reflection phases remain constant for a certain time duration. It is worth noting that all methods described earlier are also valid for the case of high mobility if the RIS reflection phases can be tuned in real-time with a sufficiently high rate. However, in practice, due to limitations in terms of the RIS design and signaling overhead in the network, the RIS reflection phases can be tuned at only (certain) discrete-time instants. Let us denote the RIS reconfiguration interval by t_r (in seconds), i.e., the RIS phases can be adjusted in every t_r seconds only. In our first computer simulation, we consider that the complex envelope is represented by its samples taken at every t_s seconds. Here, we assume that once the RIS reflection phases are adjusted according to the LOS path, they remain fixed for Qt_s seconds. In other words, for $Q = 1$, we update the RIS reflection phases at each sampling time and obtain the results given throughout the paper. In **Figure S16A**, we perform this simulation for the high mobility case of $V = 100$ m/s, $f_c = 3$ GHz and $t_s = 3.125$ μs with $N = 1$ and $M = 0$ (for the basic scenario of **Figure 1**). Here, t_s has been intentionally reduced to capture the variations in the complex envelope with respect to time due to the higher Doppler spread of the unmodulated carrier and a travel distance of 3λ is considered. In this case, we assume that RIS reflection phases are modified as $\theta(t) = -4\pi f_D t \pmod{2\pi}$ in every Qt_s seconds, i.e., the RIS cannot be reconfigured fast enough compared to the sampling frequency (variation) of the complex envelope. As seen from **Figure S16A**, a distortion is observed in the complex envelope due to the delayed reconfiguration of RIS reflection phases. However, we conclude that even if with $Q = 50$, the variation in the complex envelope is not as significant as in the case without an RIS (shown in the figure as a benchmark), while the variation is not significant for $Q = 20$. In what follows, we present a theoretical framework to describe this phenomenon.

In mathematical terms, for the considered scenario that is formulated by (4) in terms of its received complex envelope, assuming that the RIS reflection phase is adjusted and fixed at time instant t_1 while focusing on the complex envelope at time $t_2 > t_1$, we obtain

$$
\begin{aligned}
r(t_2) &= \frac{\lambda}{4\pi} \left(\frac{e^{-j2\pi f_D t_2}}{d_{\text{LOS}}} + \frac{e^{j2\pi f_D t_2 + j\theta(t_1)}}{d_{\text{LOS}} + 2d_1} \right) \\
&= \frac{\lambda e^{-j2\pi f_D t_2}}{4\pi} \left(\frac{1}{d_{\text{LOS}}} + \frac{e^{j4\pi f_D \Delta t}}{d_{\text{LOS}} + 2d_1} \right)
\end{aligned}
\tag{S11}
$$

where $\Delta t = t_2 - t_1 < t_r$. Here, we considered the fact that the RIS reflection phase is fixed at time t_1 as $\theta(t_1) = -4\pi f_D t_1$. As a result, we observe a variation in the complex envelope magnitude, which is a function of both f_D and Δt. It is worth noting that letting $\Delta t = 0$ in (S11), one can obtain (5) for $t = t_2$. After simple manipulations, the magnitude of the complex envelope is calculated as

$$
|r(t_2)| = \left(\frac{\lambda}{4\pi} \right) \left(\frac{1}{d_{\text{LOS}}^2} + \frac{1}{(d_{\text{LOS}} + 2d_1)^2} + \frac{2\cos(4\pi f_D \Delta t)}{d_{\text{LOS}}(d_{\text{LOS}} + 2d_1)} \right)^{1/2}.
\tag{S12}
$$

It is evident from (S12) that the magnitude of the complex envelope is no longer constant unless $4\pi f_D \Delta t \ll 1$. In light of the above analysis, to ensure a constant magnitude for the complex envelope, that is, to eliminate the fade pattern due to Doppler spread, we must have $t_r < \frac{1}{40\pi f_D}$ for the considered scenario. In other words, the RIS should be tuned fast enough compared to f_D to capture the variations of the received signal. To illustrate this effect, in **Figure S16B**, for a fixed t_r value of 12.5 μs, we change the velocity of the MS and observe the magnitude of the complex envelope. As seen from **Figure S16B**, while the smaller Doppler frequency of 500 Hz ($V = 50$ m/s) can be captured by the RIS since $t_r < \frac{1}{40\pi f_D} = 15.91$ μs for this scenario, we observe an oscillation in the magnitude for the higher Doppler frequencies of 2 kHz ($V = 200$ m/s) and 4 kHz ($V = 400$ m/s) since the condition of $t_r < \frac{1}{40\pi f_D}$ is no longer satisfied. In light of the above discussion, we conclude that increasing Doppler frequencies poses a much bigger challenge for the real-time adjustment of RIS reflection phases.

Finally, it is worth noting that in case of slow fading ($1/f_D \gg T_s$), where T_s is the symbol duration, the channel may be assumed to be static over one or several transmission intervals and the variations in the magnitude of the complex envelope from symbol to symbol (in our case, for unmodulated cosine signals) can be compensated by adjusting RIS reflection phases at every T_s seconds (with slight variations in magnitude if $T_s > \frac{1}{40\pi f_D}$). On the other hand, in the case of fast fading ($1/f_D < T_s$), since the channel impulse response changes rapidly within the symbol duration, in order to compensate Doppler and fading effects, i.e., to obtain a fixed magnitude for the complex envelope during a symbol duration, RIS reflection phases should be tuned at a much faster rate compared to T_s. As an example, consider the transmission of an unmodulated cosine signal for a period of 3 ms as in **Figure S16A**. For this case, we have fast fading due to the large Doppler spread, and this can be eliminated by adjusting the RIS reflection phases at a much faster rate compared to 3 ms, i.e., $t_r < 7.96$ μs. Failure of doing this causes variations in the complex envelope magnitude as shown in **Figure S16A**.

APPENDIX

The received complex envelope in (S2) can be expressed as

$$r(t) = r_{\text{LOS}}e^{j\xi_{\text{LOS}}(t)} + r_1 e^{j\xi_1(t)} + r_2 e^{j\xi_2(t)} \tag{S13}$$

where magnitude and phase values of the LOS and two reflected signals (from IO 1 (RIS) and IO 2) are shown by r_{LOS}, r_1, r_2 and $\xi_{\text{LOS}}(t)$, $\xi_1(t)$, $\xi_2(t)$, respectively. Here, we are interested in the maximization of $|r(t)|$ with respect to $\xi_1(t) = 2\pi f_D t + \theta_1(t)$, which captures the reconfigurable reflection phase of the RIS. We use the following trigonometric identity: For $z_1 = r_1 e^{j\xi_1}$, $z_2 = r_2 e^{j\xi_2}$, $z_3 = r_3 e^{j\xi_3}$, and $z_4 = z_1 + z_2 + z_3 = r_4 e^{j\xi_4}$, we have $r_4 = (r_1^2 + r_2^2 + r_3^2 + 2r_1 r_2 \cos(\xi_1 - \xi_2) + 2r_1 r_3 \cos(\xi_1 - \xi_3) + 2r_2 r_2 \cos(\xi_2 - \xi_3))^{1/2}$. In light of this, the maximization of $|r(t)|$ can be formulated as

$$\max_{\theta_1(t)} |r(t)|^2$$

$$\max_{\theta_1(t)} r_{\text{LOS}}r_1 \cos(\xi_{\text{LOS}}(t) - \xi_1(t)) + r_1 r_2 \cos(\xi_1(t) - \xi_2(t))$$

$$\max_{\theta_1(t)} r_{\text{LOS}} \cos(4\pi f_D t + \theta_1(t))$$

$$+ r_2 \cos(2\pi f_D t(1 - \cos\alpha) + \phi_2 + \theta_1(t)) \tag{S14}$$

where the constant magnitude terms and the term does not contain $\theta_1(t)$ is dropped. Using the identity $\cos(x + y) = \cos x \cos y - \sin x \sin y$ and grouping the terms with $\theta_1(t)$, we obtain

$$\max_{\theta_1(t)} \; A \cos \theta_1(t) + B \sin \theta_1(t)$$

$$\max_{\theta_1(t)} \; \operatorname{sgn}(A) \sqrt{A^2 + B^2} \cos(\theta_1(t) + \tan^{-1}(-B/A)) \tag{S15}$$

where A and B are as defined in (S5) and the harmonic addition theorem is used. Consequently, to maximize the complex envelope, we have to ensure

$$\operatorname{sgn}(A) \cos(\theta_1(t) + \tan^{-1}(-B/A)) = 1. \tag{S16}$$

This can be satisfied by

$$\theta_1(t) = \frac{\pi}{2}(1 - \operatorname{sgn}(A)) - \tan^{-1}(-B/A) \tag{S17}$$

which completes the proof.

REFERENCES

Goldsmith, A. (2005). *Wireless Communications* (Cambridge, UK: Cambridge University Press)

Liu, F., Tsilipakos, O., Pitilakis, A., Tasolamprou, A. C., Mirmoosa, M. S., Kantartzis, N. V., et al. (2019). Intelligent metasurfaces with continuously tunable local surface impedance for multiple reconfigurable functions. *Phys. Rev. Applied* 11, 044024

Wu, Q. and Zhang, R. (2019). Beamforming optimization for intelligent reflecting surface with discrete phase shifts. In *Proc. 2019 IEEE Int. Conf. Acoust. Speech Signal Process. (ICASSP)* (Brighton, UK)

FIGURE CAPTIONS
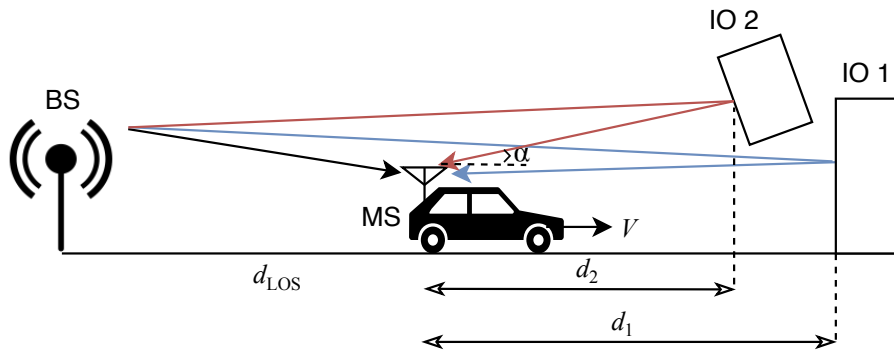
Figure S1. Propagation scenario with two IOs.
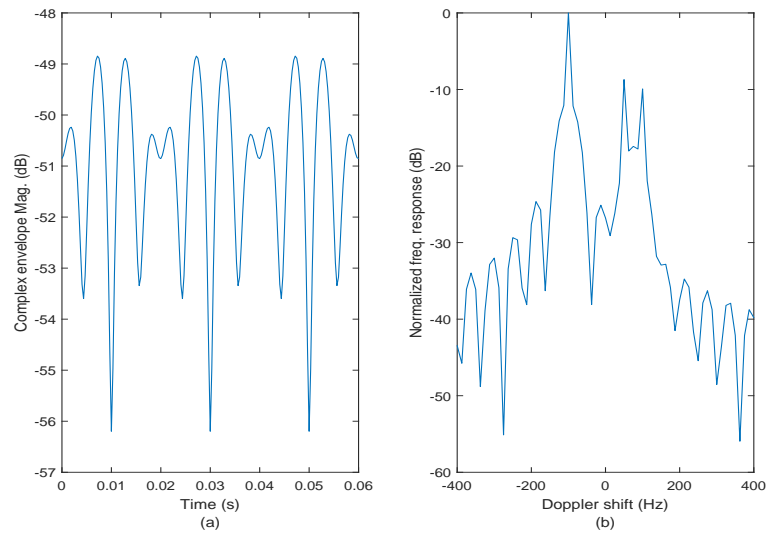
Figure S2. The scenario of **Figure S1** without an RIS: (a) Complex envelope magnitude, (b) Doppler spectrum of the received signal.
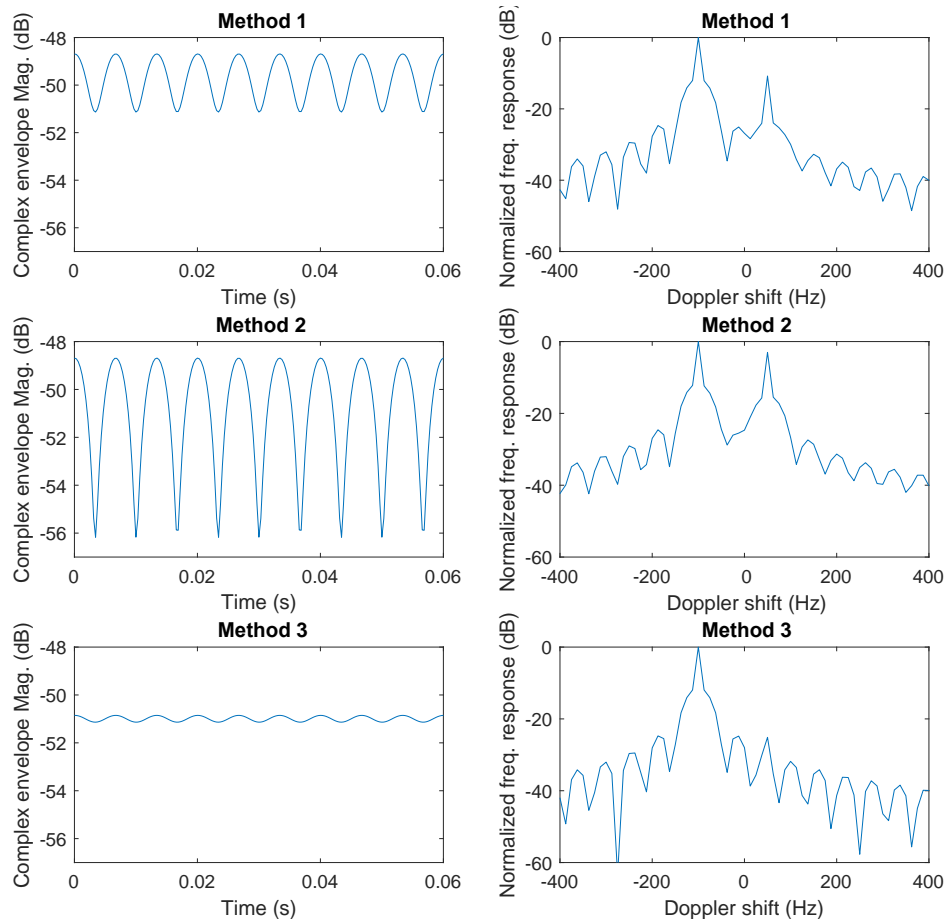
Figure S3. Magnitude and Doppler spectrum of the received signal with an RIS for scenario of **Figure S1** under three different phase selection methods.
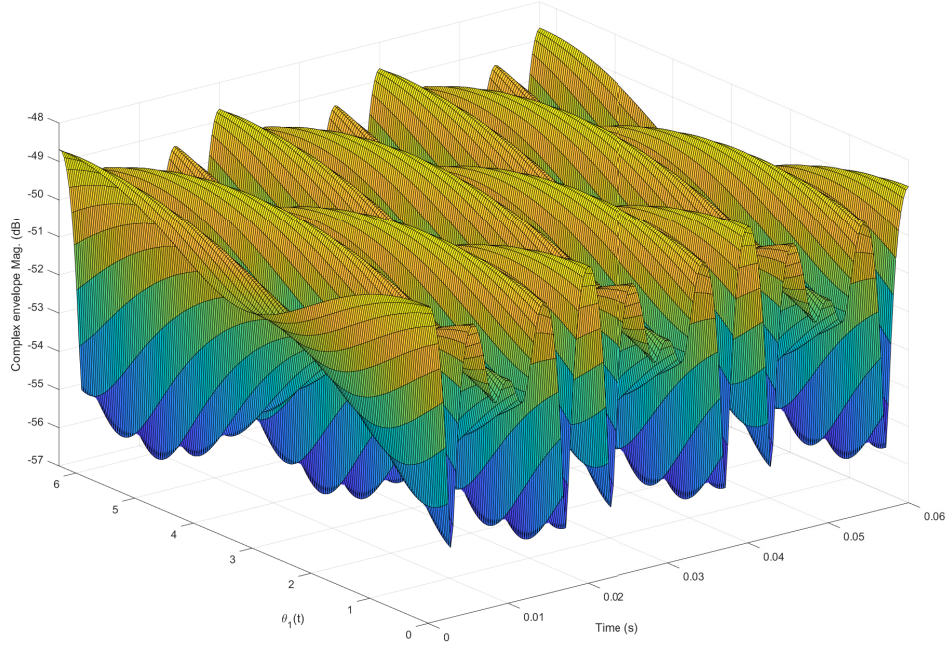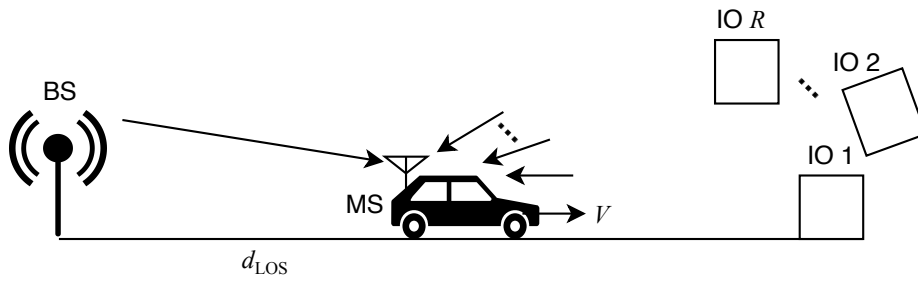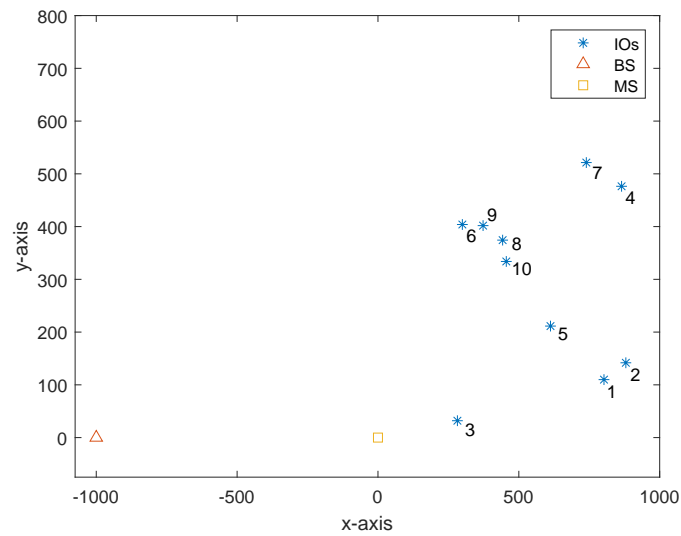
Figure S4. 3D illustration of the variation of the complex envelope magnitude with respect to time for all possible RIS reflection angles (scenario of **Figure S1**).
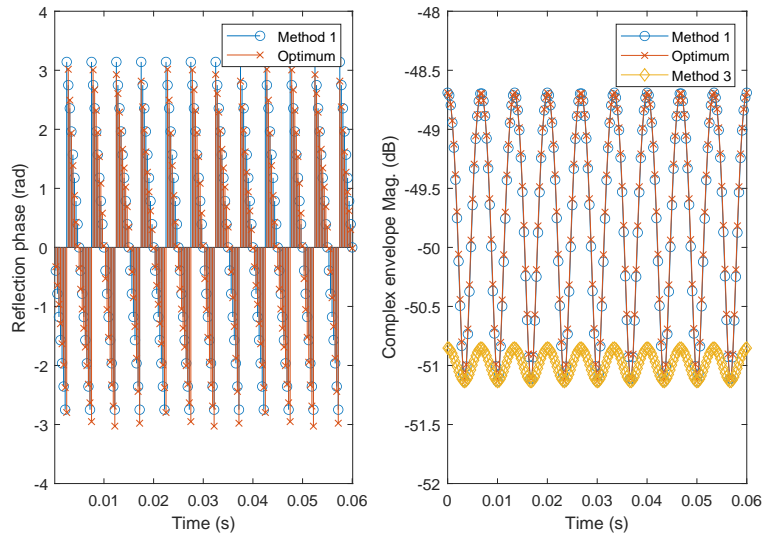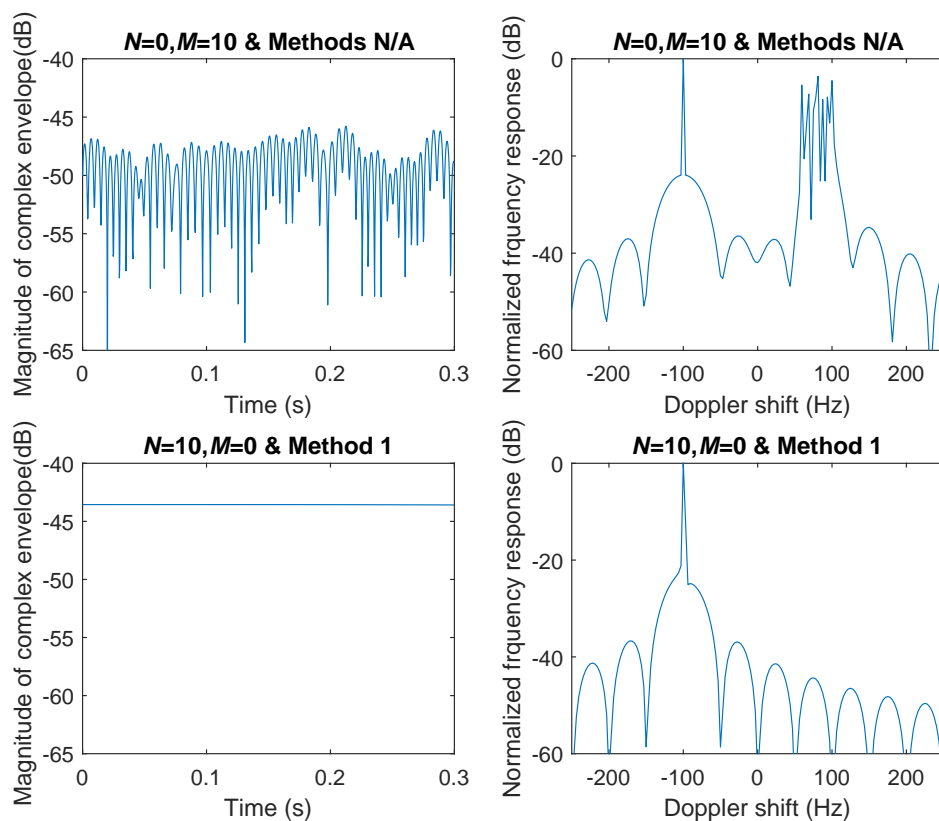

Figure S5. Comparison of reflection phases and complex envelope magnitudes for Method 1 and the optimum method.

Figure S6. The general case of multiple IOs with N RISs and M plain IOs ($R = N + M$).

Figure S7. Considered simulation geometry with multiple IOs (the first N of them are assumed to have RISs).

Figure S8. Complex envelope and Doppler spectrum for two extreme cases under the scenario of **Figure S6**: (top) $N = 0, M = 10$ (10 plain IOs without any RISs) and (bottom) $N = 10, M = 0$ (10 RISs without any plain IOs).
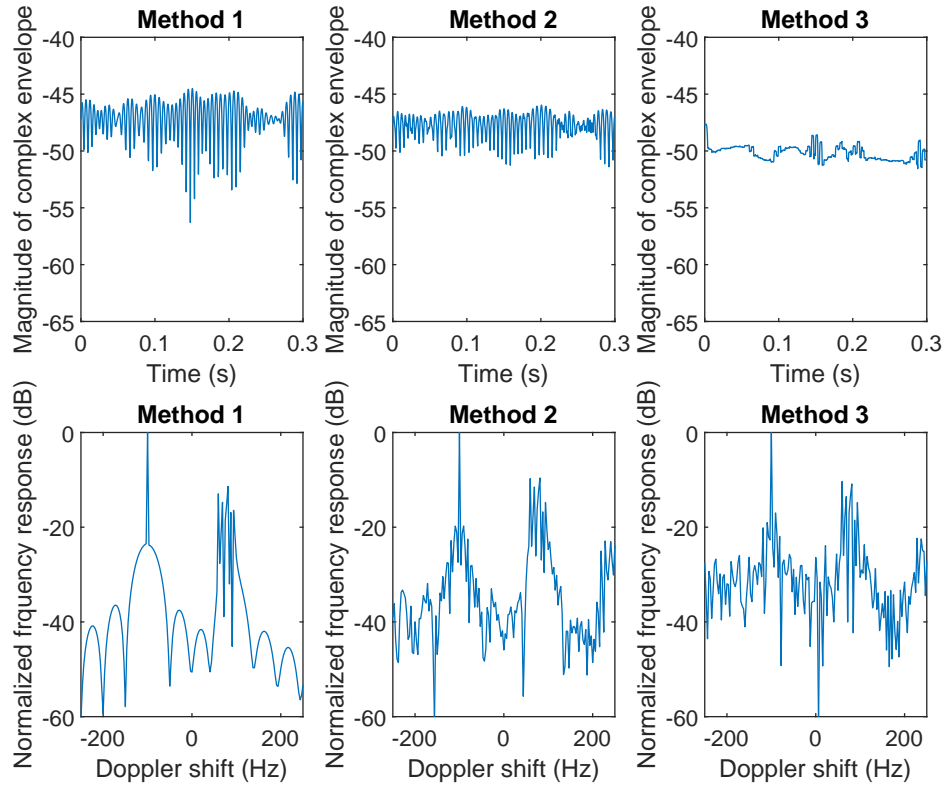
Figure S9. Complex envelope magnitude and Doppler spectrum for the general case with 10 IOs and $N = 3, M = 7$ (Setup I).
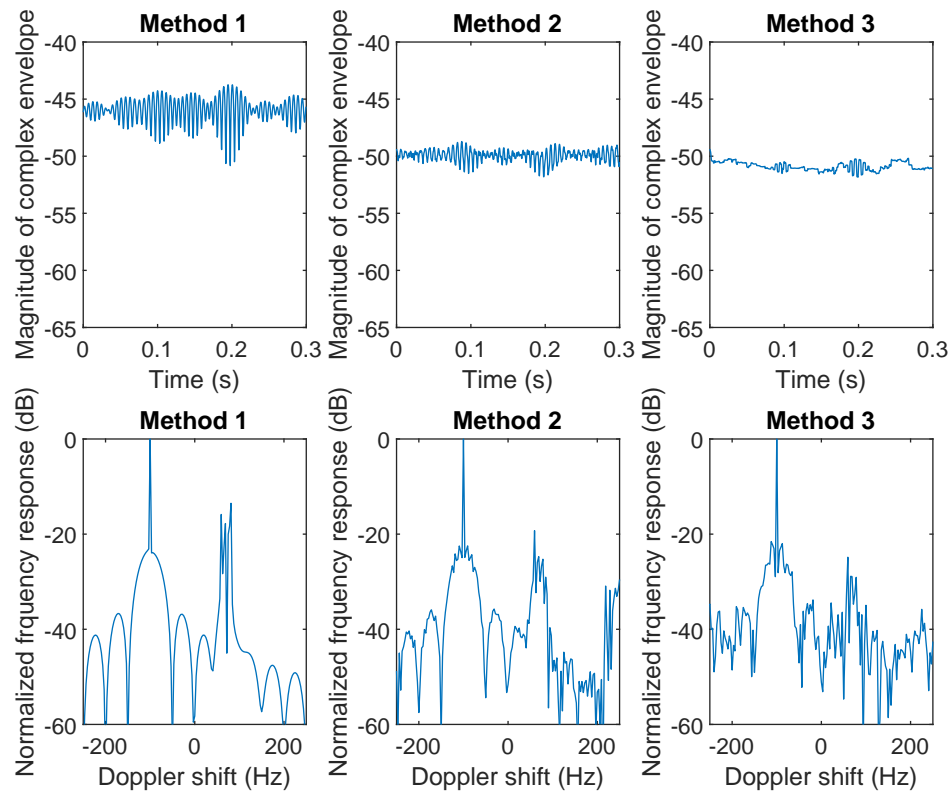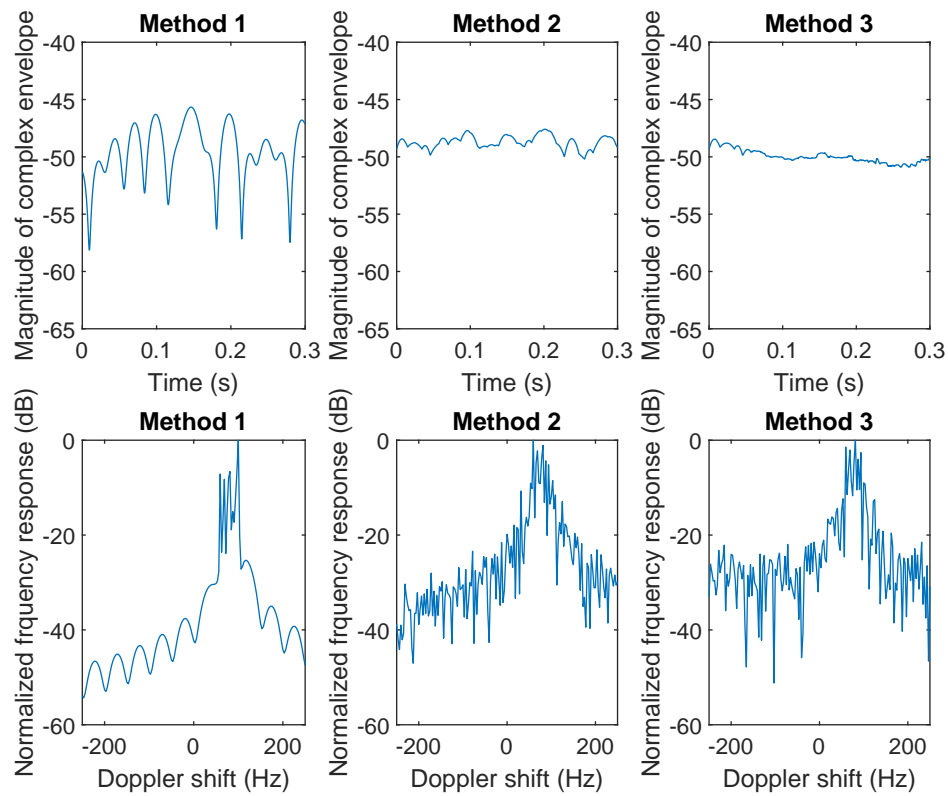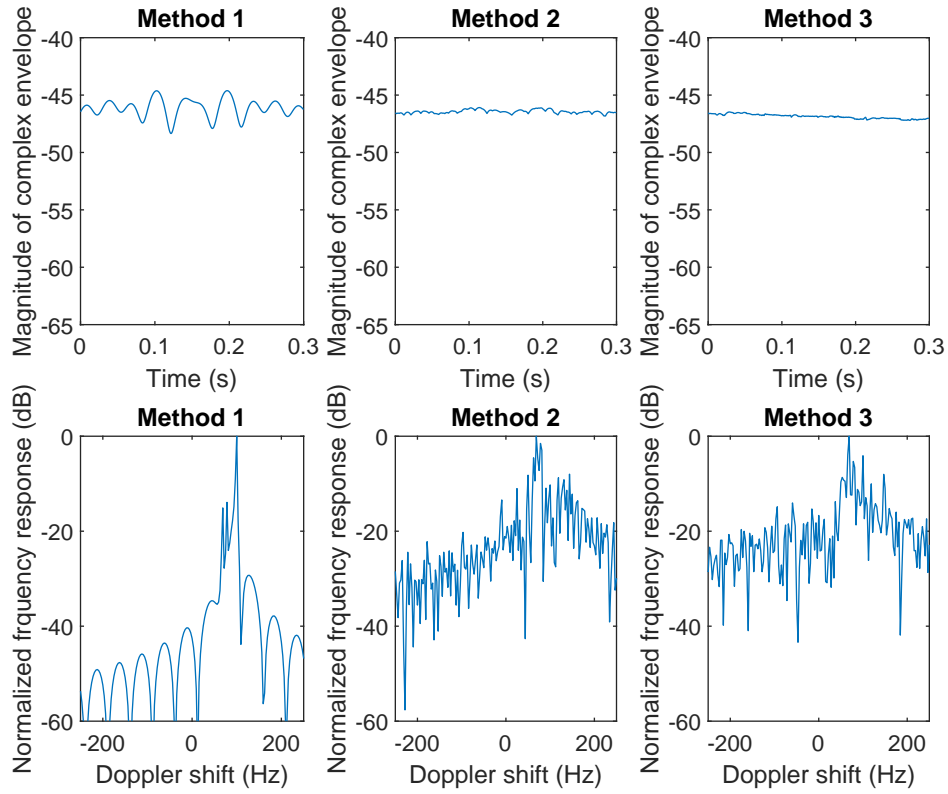
Figure S10. Complex envelope magnitude and Doppler spectrum for the general case with 10 IOs and $N = M = 5$ (Setup I).
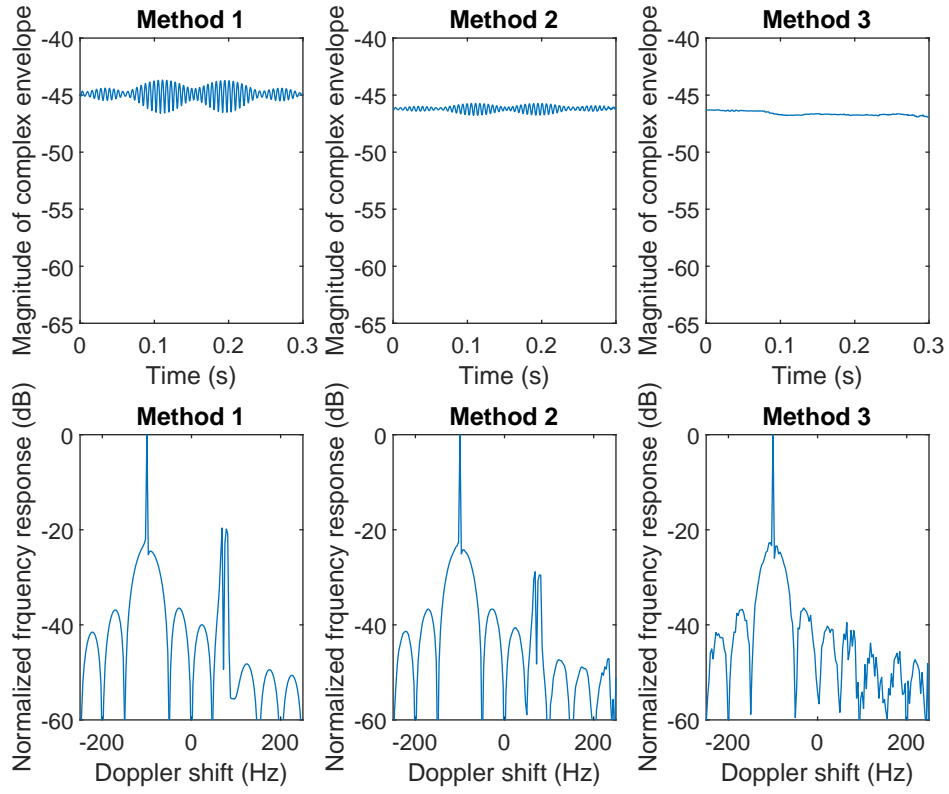
Figure S11. Complex envelope magnitude and Doppler spectrum for the general case with 10 IOs and $N = 7, M = 3$ (Setup II).
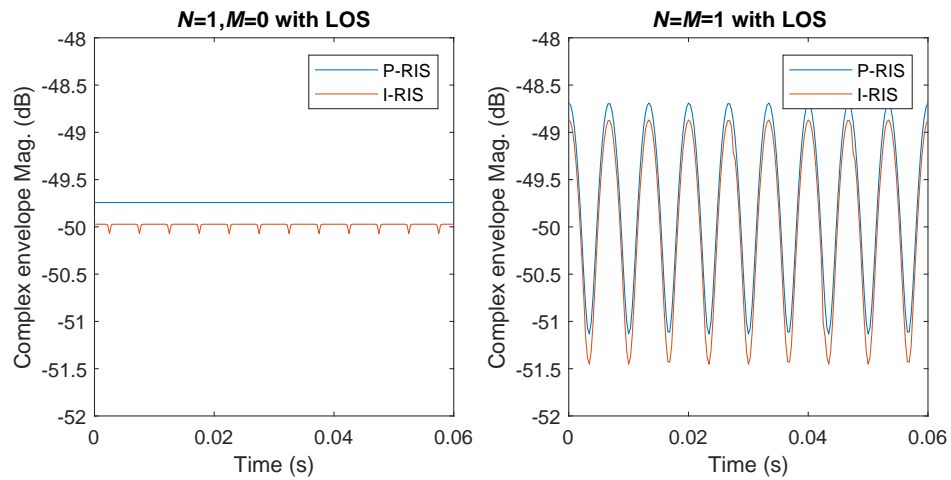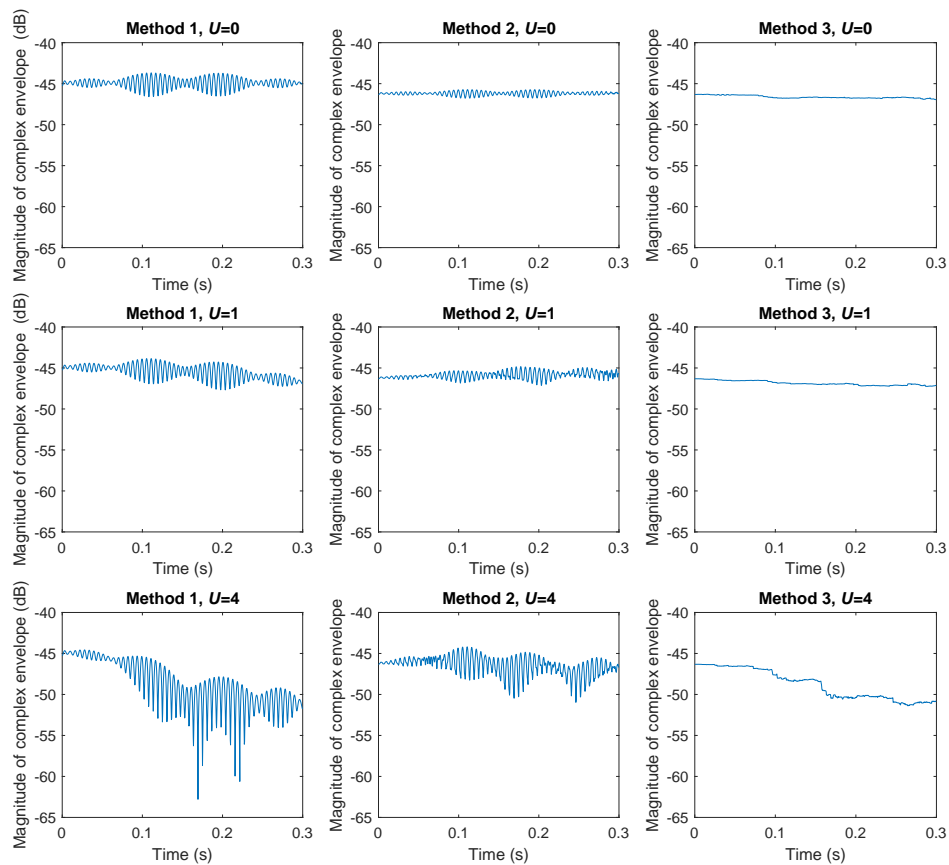
Figure S12. Complex envelope magnitude and Doppler spectrum for the general case with 10 IOs without a LOS path and $N = 3, M = 7$ (Setup I).
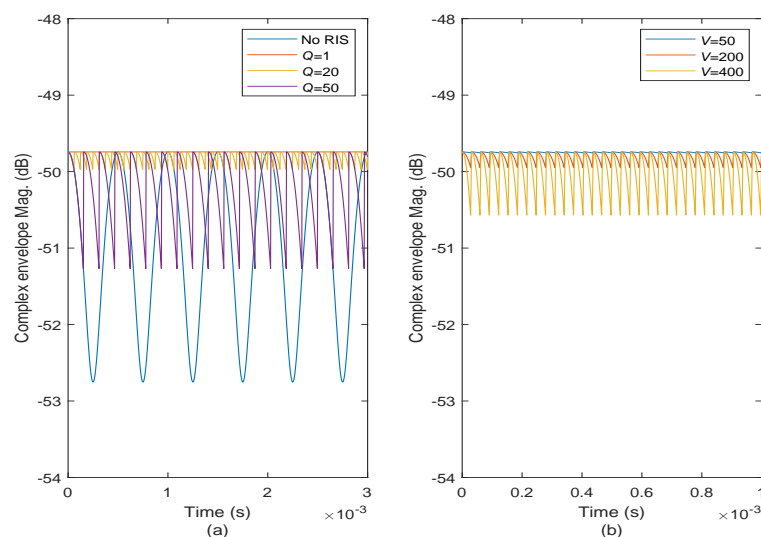
Figure S13. Complex envelope magnitude and Doppler spectrum for the general case with 10 IOs without a LOS path and $N = 7, M = 3$ (Setup II).

Figure S14. Complex envelope magnitude in the presence of a realistic RIS for the scenarios of **Figures 1,S1**.

Figure S15. Complex envelope magnitude for the general case with 10 IOs with a LOS path and $N = 7, M = 3$ under erroneous Doppler frequency shifts at RISs ($U = 1$ and 4) with the perfect case ($U = 0$).

Figure S16. Complex envelope magnitude for the scenario of **Figure 1** ($N = 1, M = 0$) a) under high mobility ($V = 100$ m/s) and fixed reflection phases for a period of Qt_s seconds with $Q = 1, 20,$ and $50,$ b) under increasing Doppler frequencies and a reflection phase update duration of $t_r = 12.5$ μs.